Irreversible Effects in Thin Film Buckling and Development of a High Temperature Thermoplastic Foam

by

Junyu Yang

Bachelor of Engineering, Dalian University of Technology, 2013

Submitted to the Graduate Faculty of the

Swanson School of Engineering in partial fulfillment

of the requirements for the degree of

Doctor of Philosophy

University of Pittsburgh

2020

UNIVERSITY OF PITTSBURGH

SWANSON SCHOOL OF ENGINEERING

This dissertation was presented

by

Junyu Yang

It was defended on

November 25, 2019

and approved by

Lei Li, Ph.D., Associate Professor, Department of Chemical and Petroleum Engineering

Tagbo Niepa, Ph.D., Assistant Professor, Department of Chemical and Petroleum Engineering

Markus Chmielus, Ph.D., Assistant Professor, Department of Mechanical Engineering and Materials Science

Dissertation Director: Sachin Velankar, Ph.D., Associate Professor, Department of Chemical and Petroleum Engineering

Irreversible Effects in Thin Film Buckling and Development of a High Temperature Thermoplastic Foam

Junyu Yang, PhD

University of Pittsburgh, 2020

Three projects in total are involved in this dissertation. They are: (1) Compression-induced fold localization of thin films bonded to viscous substrate. (2) Stretching-induced wrinkling in plastic-rubber composites. (3) The preparation and thermomechanical properties of high temperature PPEK foams.

In the study of irreversible effects in the thin film buckling. Two projects would be covered: (1) Compression-induced fold localization of thin films bonded to viscous substrate. The basic idea is as following: the viscous liquid is layered on a prestretched rubber substrate, and a strip of film is then placed on the surface of the liquid. Releasing the rubber substrate at a well-controlled rate imposes compressive stress on the liquid, which in turn compresses the film and induces buckling at the free surface. In this project, the following work would be discussed in detail: 1) how the experiments are implemented: set up of the self-designed experiments and digital image correlation (DIC) analysis approach for video data processing; 2) analysis the effect of releasing rate of the rubber and liquid layer thickness to the system. (2) Stretching-induced wrinkling in plastic-rubber composites. In this study, the mechanics of three-layer composite films composed of an elastomeric layer sandwiched between two thin surface layers of plastic is studied. Upon stretching and releasing such composite films, they develop a highly wrinkled surface texture. High aspect ratio wrinkles – with the amplitude to wavelength ratio

exceeding 0.4 – can be realized. Also, with help of simulation, the effect of plasticity of the face layers has been studied in this project.

At last, In the study of the preparation and thermomechanical properties of high temperature PPEK foams, the following work will be shown in detail: 1) develop a foaming process to convert phthalazinone-based polymers into foams of various densities; 2) evaluate the density, microstructure, mechanical and thermal properties of the foams. And specifically, thermal conductivity and modulus of the foam will be measured as a function of their density.

Table of Contents

List of Tables

List of Figures

Preface

Foremost, I would like to express my sincere gratitude to my research advisor, Professor Sachin Velankar, for his support over the past five years. I would like to thank him for his contributions of time, ideas and funding to make my Ph.D. experience productive and stimulating. As a great mentor for me, Professor Velankar always showed me his patience, diligence and painstaking attention to research, which encourages me a lot in my Ph.D life.

I want to acknowledge Professor Chmielus , Professor Li, and Professor Niepa, for serving as my committee members. I would like to thank them for their insightful comments and suggestions.

I would like to thank to all of my colleague members and collaborators, including Brian Young, Junyi Yang, Derrick Amoabeng, Ya Gao, Yi Zhang, Sameer Damle, Eshwar Hamesh and Anantha Padmanabha Sarma. It is my great pleasure to work with all of you and I wish you all the best. I would like to thank Dr. Susheng Tan and Mike McDonald for training me on Scanning Electron Microscope (SEM).

At last, I’m grateful to my mom and my relatives for their support and encourage for me over these years of my Ph.D life.

1.0 Introduction

In this dissertation, three projects will be included that cover two topic areas. The two topics are: (i) the study of irreversible effects in thin film buckling and (ii) the development of high temperature thermoplastic foam.

A thin stiff elastic film bonded to a softer elastic substrate can buckle to form wrinkle patterns when subjected to compressive stress. The past decade has seen numerous articles in this area exploring the fundamental mechanics of such buckling.[1-4] A large majority of research has examined elastic systems, i.e. the thin film as well as the soft substrate were treated as elastic (often linearly elastic) materials[1, 3, 5, 6]. But materials used in experiments or of interest to practical applications have more complex material properties, and there is now a growing literature on thin film wrinkling when the substrate or film is an inviscid liquid[7-9], viscous liquid[10-13] viscoelastic[14-16], capable of yielding[17-19], or softening upon increasing temperature[20]. It is in this spirit that the topic in this dissertation examines the irreversible deformation and wrinkling behavior of thin films within different systems. In this area of irreversible effects in thin film buckling, two projects are covered.

The first is compression-induced fold localization of thin films bonded to viscous substrate. The basic idea is as following: a viscous liquid is layered on a prestretched rubber substrate, and a strip of film is then placed on the surface of the liquid. Releasing the rubber substrate at a well-controlled rate imposes compressive stress on the liquid, which in turn compresses the film and induces buckling at the free surface. The aim of this project is to study the wrinkling conditions for the system and also better understand the wrinkling to folding transition phenomenon. Specifically, the following work would be discussed in detail: 1) how the experiments are implemented: set up of the self-designed experiments and digital

image correlation (DIC) analysis approach for video data processing; 2) analysis the effect of releasing rate of the rubber and liquid layer thickness to the system.

The second topic on irreversible effects in thin film wrinkling concerns stretching-induced wrinkling in plastic-rubber composites. The overall goal of this project is to examine the mechanics of three-layer composite films composed of an elastomeric layer sandwiched between two thin surface layers of plastic. Upon stretching and releasing such composite films, they develop a highly wrinkled surface texture. The stretching of the initially smooth composite films leads to a geometric mismatch: since the plastic layers yield during stretching, the stress-free length of the plastic layers is longer than that of the elastomeric midlayer. Upon releasing, the film develops an internal stress, and the face layers undergo compression-induced buckling, resulting in a heavily wrinkled surface. High aspect ratio wrinkles – with the amplitude to wavelength ratio exceeding 0.4 – can be realized. Also, with help of simulation, the effect of plasticity of the face layers has been studied in this project.

Finally, we turn to a different area of the preparation and thermomechanical properties of high temperature Poly (phthalazinone ether ketone) (PPEK) foams. High temperature foam (HTF) a category of foams made out of high-performance polymers (HPPs) that can endure relatively high continuous working temperature. Intrinsically, all the polymers that were used to make into HTFs require either polymers with high T_g, or semi-crystalline polymers with a high melting point, or crosslinking. The density of PPEK is 1.35 g/cm^3 and has a relatively high T_g about 263°C. The high T_g of PPEK potentially makes it a promising material for preparing HTF. The objective of this research is to prepare a new kind of high temperature foam from PPEK. Specifically, the following will be shown in detial: 1) develop a foaming process to convert phthalazinone-based polymers into foams of various densities; 2) evaluate the density, microstructure, mechanical and thermal properties of the

foams. Also, foam survivability has been confirmed with high working temperature as high as 200°C.

The thermomechanical properties of phthalazinone-based foams, specifically thermal conductivity and modulus are measured as a function of their density (i.e. as the void content in the foam increases), and the density range will be target roughly from 0.1g/cm^3 to 0.7g/cm^3 (the corresponding volume fractions range from 48% to 93%).This portion of the research is the primary goal of this project.

2.0 The Preparation and Thermomechanical Properties of High Temperature PPEK Foams

2.1 Introduction

Porous polymeric materials made especially from high performance polymers (HPPs), which may have some superior properties in many aspects of view, such as mechanical, thermal, chemical as well as physical. Typical applications of these materials include structural materials for aerospace and automotive, electronics, capacitors, batteries, fuel cells, and medical implants, etc. [21-25]

High temperature foams (HTFs) a category of foams made out of HPPs that can endure relatively high continuous working temperature. Intrinsically, all the polymers that were used to make into HTFs require either polymers with high T_g, or semi-crystalline polymers with a high melting point, or crosslinking. For example, the T_g of polysulfone (PSU) is around 187°C [26] and the T_g of polyether ether ketone (PEEK) is about 143 °C [27], etc. A high glass transition temperature for the polymer could potentially promise the foam product that may work at a relatively high temperature, i.e. high polymer T_g or crosslinking or melting temperature is the necessary condition for the HTFs.

Numerous different polymer foams are available commercially, e.g. polystyrene and polyethylene, (which dominate the low-cost market), or polyurethanes (used in higher value applications such as refrigerator insulation). However, most of these cannot withstand high temperatures, and hence are unsuitable for structural or insulation applications where high temperatures are encountered, e.g. for under-the-hood structural parts in the automobile industry, or high temperature insulation in the chemical industry. HTFs may include polyurethane and epoxy-urethane foams [28, 29]; polymethacrylimide (PMI) foams [30];

silicone foams [31]; melamine foam [32]; polyimide foams [33, 34]; polyvinyl chloride foams [35] and polyamide and polyvinylidene fluoride foams [36]. Some tradenames, manufacturers, and key technical information about such foams is presented in Table 1 in Appendix A. Also, a review paper that is focused on HTFs and their properties has been written out and under revision right now, which will be submitted soon.

This project concerns foams made from phthalazinone-based thermoplastic polymers (Poly (phthalazinone ether sulfone) (PPES), Poly (phthalazinone ether sulfone ketone) (PPESK) & PPEK, see structures in Fig. Appendix A.1). The main characteristics of the PPES, PPEK, PPESK are heat resistance, soluble, high strength and anti-abrasion. [37]. These properties make these novel HPP materials promising with a wide range of potential applications.

The HPP of interest here is PPEK (structure shown below in Fig 2.1). Its density is 1.35 g/cm^3 and has a relatively high T_g about 263°C.

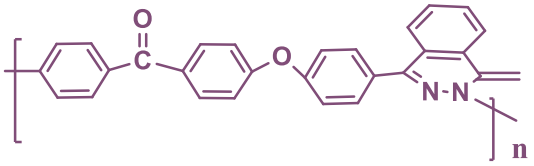

Figure 2.1. Chemical structure of Poly (phthalazinone ether ketone) (PPEK)

Based on literature study, PPEK may have some rivals to compete with in the field of HTF. The obvious competitors to phthalazinone-based polymers may be polyaryletherketone (PAEK)s, poly(ether ketone ketone) (PEKK) and poly(ether ether ketone) (PEEK) etc. They have superior mechanical properties, thermal and chemical stability, as well as unique physical properties[38-40]. Significant applications of these high-performance polymers include electronics, structural materials for aerospace and automotive, capacitors, batteries,

fuel cells, and medical implants [41-46]. Intrinsically, PEEK and PEKK have a T_g range from 136°C to 156°C. The limitation of these foams may as follows: 1) hardly have them work with temperature beyond 170° C. 2) hard to prepare foam with low density, for example, less than 0.4g/cm^3. [21, 27, 47, 48] The reason for this difficulty might be that PEEK and PEKK are semi-crystalline polymers, whose heat distortion temperature are few tens degrees lower than their T_g, In general, bubble nucleation and foam growth requires heating to above at least T_g, but then several ten degrees of cooling is required to bring the polymer below heat distortion temperature after foaming. This cooling time plus the nature of their low melt strength, permits foam collapse, especially in thick foam parts that cool slowly because foams have a low thermal conductivity.

Next comes the ones of the most commonly used special engineering plastics: polysulfone (PSU), polyphenylsulfone(PPSU) and poly(arylene ether sulfone) (PAES). They have outstanding properties, for instance, high modulus, lightweight, strength and hardness, and especially an intrinsic flame-retardant property. In addition, it also has outstanding thermal stability and remarkable aging resistance. Therefore, there is a broad application prospect for them in many fields, such as in aerospace, the automotive industry, insulation materials, microelectronics packaging, flexible circuit boards and other high-tech fields.[49-52] Intrinsically, PSU and PAES foam have a T_g higher than 152°C [25, 26, 53, 54]and PPSU foam as high as 219°C[55]. However, these foams are usually pricy.

Finally polyimide (PI) foams have attracted increasing attention in the last decades because of their unique properties, such as good thermal and acoustic insulation, high thermal stability, and excellent fire resistance. At present, PI foams have been widely applied in the fields of spacecraft, aircraft, marine, and high-speed trains [56-59]. Intrinsically, PI has a relatively high T_g, i.e. above 400°C, making its the long-term service temperatures of most polyimide foams as high as 300°C.[60] The limitation of PI foams may lie in the

complication of preparation process, i.e. complex reactions and various chemicals may involve during the of foam precursors preparation and foaming process. [60-62]

In this project, blowing agent-assisted foaming techniques has been used to prepare PPEK foams. This foaming technique typically uses the gas resulting from either thermally decomposable or expandable chemicals, i.e. blowing agent, to nucleate and grow the cavities within the polymer matrix. In particular, thermally expandable gases, such as CO_2, have attracted more attention in recent years due to their nontoxicity and precise control of porous structures [47, 63-65]. This foaming technique is carried out in pre-molded solid polymeric materials; thus, in many cases, this is also called "solid state foaming" method. The polymeric materials are first saturated with inert gas at an elevated pressure (e.g., 0.5MPa to 12MPa for polysulfone [26, 53, 54], polyphenylsufone (PPSU)[55, 63] and poly(arylene ether sulfone)(PAES) [25]) from a few hours[25] to several days [53], followed by expanding the gas in saturated polymers at high temperature (usually around glass transition temperature). This technique has been successfully applied to various HPPs, including polyetherimide[64, 66-69], polyethersulfone [64, 68, 69], and polyetheretherketone[27, 48, 65], with precisely controlled pore size from nano-to-macroscale. For the nature of the polymer, the chain structures are usually rigid and the glass transition temperatures are consequently high. Thus, high temperature and pressure, as well as long foaming periods are necessary for the purpose of saturation the polymer matrix with gaseous blowing agent[70-72].

For controlling the cell morphology (namely, the number of cells, the cell size, and its distribution) in thermoplastic foams and thereby improve foam quality[73], nucleating agent has been added into our foam system. Talc, an inexpensive particulate material is widely used nucleating agent in foaming industry[74]. For preparing nucleating agent added samples, talc power (<5wt%) is well mixed with PPEK powder before platen press molding. Detailed preparation procedure will be shown in later section.

2.2 Experimental section

2.2.1 Materials

Phthalazinone ether ketone (PPEK) powder, ρ≈1.35 g/cm3, T_g≈ 261°C and Mn≈ 18816 was synthesized and supplied by Join King Fine Chemical Co., Ltd. Dichloromethane (DCM), heptane (lab grade) and talc fine powder (ACROS Organics™) were purchased from Fisher Science. Glycerin (technical grade), PIT process chemicals, was purchased from Mcmaster. Glycerin works as the contact lubricant for thermal conductivity measurement[75].

PPEK with talc were prepared using a Brabender Electronic Plasti-Corder Mixture (model number EPL-V5501). It operates on the counter rotation of two roller blades, which induces strong shear forces for efficient mixing of the blends. The maximum mixer capacity with the roller blades installed is 60 mL. 50g of PPEK powder and talc powder (about 5% in weight) were added one after another while blending at 92 rpm for 5 min under 260°C.

2.2.2 PPEK Foaming Process

The melt-blended sample is first converted into a thick plaque using compression molding with a platen press. Flat sheets of typical thickness 0.6 mm and lateral dimensions of several cm were made.

Portions of these plaques were cut into rectangular shapes of roughly 20mm*30mm and immersed into a solution (see below) which contained the blowing agent. The discs then absorbed the blowing agent. After the desired immersion time, the disc was withdrawn from the solution and immediately converted into a foam by immersing it into a heating bath that had been set to the desired foaming temperature. For thermal and mechanical tests, a metal

foaming case, which sandwiches the disk between two plates held apart at a fixed distance, 3mm in most cases for foam preparation in this project, is applied to prepare flat and uniform-thickness foam samples. After foam expansion for the desired time, the discs were withdrawn and cooled in air.

2.2.3 Characterizations

Density was calculated by hydrostatic weighing i.e. using the difference of the sample when weighted in air vs in water. Sections of the foam were cryo-fractured in liquid nitrogen and examined by scanning electron microscopy (SEM, JEOL JSM-6510LV/LGS, Pd coating). The main parameters of interest are the mean cell size and the number of cells per unit volume. All foams appeared to be closed cell, at least as judged visually. Differential scanning calorimetric (DSC) analysis was performed on a TA instrument DSC Q100 at a scanning rate of 10 °C min^{-1} in a nitrogen flow of 50 mL min^{-1}. Gel permeation chromatography(GPC) analysis was performed on Daojin LC-16 (chromatographic column: Shodex GPC K-803), with chloroform as mobile phase and polystyrene as reference material. Both DSC and GPC results are shown in Fig. Appendix A.2 and Fig. Appendix A.3. Indentation tests were carried out with TestResouces(200 Series Electromechanical Universal Test Machines, 5kN) with ball head indenter (4mm in diameter). The thermal conductivity of samples was measured as described later.

2.3 Results and Discussion

2.3.1 Selection of Blowing Agent

A good physical blowing agent must have high solubility into the polymer being foamed. The literature suggests that phthalazinone-based polymers are soluble in chlorinated solvents such as chloroform or dipolar aprotic solvents, such as dimethylacetamide (DMAc)[76, 77]. As a qualitative test of solvent compatibility, we tested dissolution of the PPEK powder in to a variety of solvents including DMAc, dimethyl sulfoxide (DMSO), N-Methyl-2-pyrrolidone (NMP), dichloromethane (DCM) and chloroform. Judgment of the solvents was made based on qualitative observations of how much polymer dissolved and the cloudiness of the polymer-solvent mixture. Among these solvents, DCM and chloroform were found to dissolve the PPEK almost completely suggesting that they may swell into PPEK adequately.

Preliminary tests were conducted using DCM and chloroform. For example, 0.6mm unfoamed sample disk was placed into DCM/Heptane (50%/50% in weight) solvent mixture for 3 days to let the disk reach its equilibrium. Then the disk was immersed into a hot oil bath set to 150°C for 30 seconds upon which it foamed. The same experiment was repeated with a chloroform heptane mixture, but was less successful: while a few small bubbles were nucleated, a foam was not obtained. Therefore, DCM was selected for all further experiments.

Since pure DCM is a good solvent, it can completely dissolve the polymer. To avoid this, a solvent/non-solvent single-phase mixture was prepared comprising DCM (solvent) and heptane (non-solvent). This mixture has poor solubility for the PPEK, yet PPEK discs immersed in this mixed solvent selectively absorb the DCM.

2.3.2 Composition of Swelling Solution

Discs of PPEK were immersed in DCM/heptane mixtures of various compositions at room temperature and ambient pressure. The samples were extracted periodically and weighed. Fig. 2.2 shows the change in weight gain (grams per gram of PPEK). As may be expected, the PPEK absorbs more DCM from solutions that have higher DCM content. Furthermore, the equilibration time (as judged by plateauing of the weight gain) reduces.

Limited experiments were also conducted with thicker samples. Not surprisingly, the equilibration time was longer. Further, even after several days of immersion, after foaming, the center of the disc remained unfoamed indicating insufficient swelling with DCM. Therefore all experiments below used discs of 0.6 mm thickness equilibrated for about 70 hours in 50/50 mixtures of DCM and heptane.

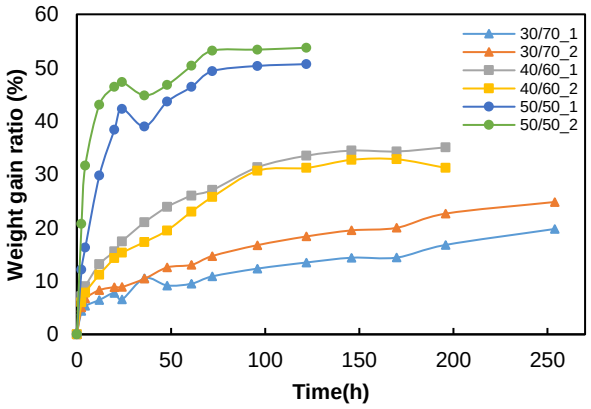

Figure 2.2. Swelling kinetics of PPEK sheets in DCM/heptane mixtures. All samples are 0.6mm thick.

2.3.3 Effect of Foaming Temperature and Foaming Time

Successful foaming requires a temperature that exceeds the glass transition temperature of the (polymer+blowing agent) mixture. While the glass transition of the PPEK is expected to be 263°C[37] , due to the large absorption of the DCM, the mixture has a much

lower glass transition temperature, as judged by the fact that samples equilibrated in more concentrated DCM mixtures become somewhat flexible. Our experiments show that foaming can proceed at temperatures between 105°C and 270°C. When immersed in an oil bath set below 105°C, foaming is not much. On the other hand, the foam easily collapses if the foaming temperature is above 270°C.

Figure 2.3 shows the effect of foaming temperature on the foam density for a fixed foaming time of 30s. We must note that these density values are average densities of the entire sample. At least some samples have a skin of unfoamed material on the surface and hence the density of the foamed region itself is likely slightly lower than these quoted values.

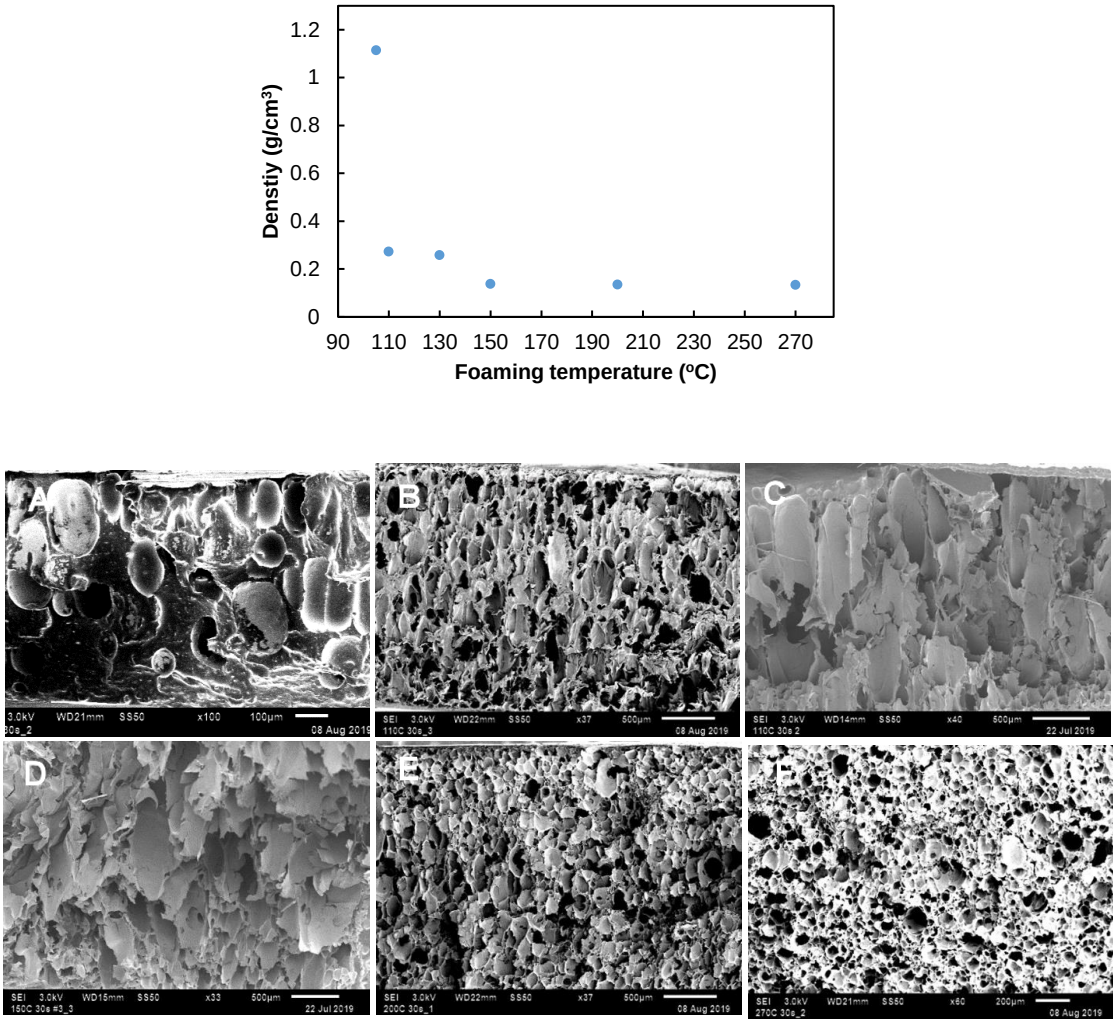

Figure 2.3. Top curve: density of 0.6mm, 30s foaming time samples with different foaming temperature: 105°C, 110°C, 130°C, 150°C, 200°C, 270°C; bottom images: cross-section of the foams from 105°C to 270°C (A to F) respectively.

For two selected temperatures, samples were foamed for foaming times ranging from few seconds to 100 seconds. The density of the foam reduces with the increasing of the foaming time as shown in Fig. 2.4 below. For samples foamed at 110°C, density decreases significantly within the first 30s of foaming, followed by almost no change at later times. We speculate that this initial foaming sharply reduces the fraction of DCM within the PPEK, so that the glass transition temperature rises above 110°C, thus preventing further foam

expansion. At 270°C, a low-density foam appears even at 10s foaming time. At long foaming times however, the density rose significantly. SEM images show: (1) shrinking for the small cells (tens of microns ones); (2) maybe coalescence of some other larger cells. This result suggests a gradual collapse of the foam since this foaming temperature well exceeds the glass transition temperature of the polymer itself.

Note that in Fig. 2.4, figure A refers to 110°C whereas the reminder to 270°C, by comparing figure A & B, it's easy to see that even under a short foaming time, i.e., 10s, 270°C sample foamed more than the 110°C sample.

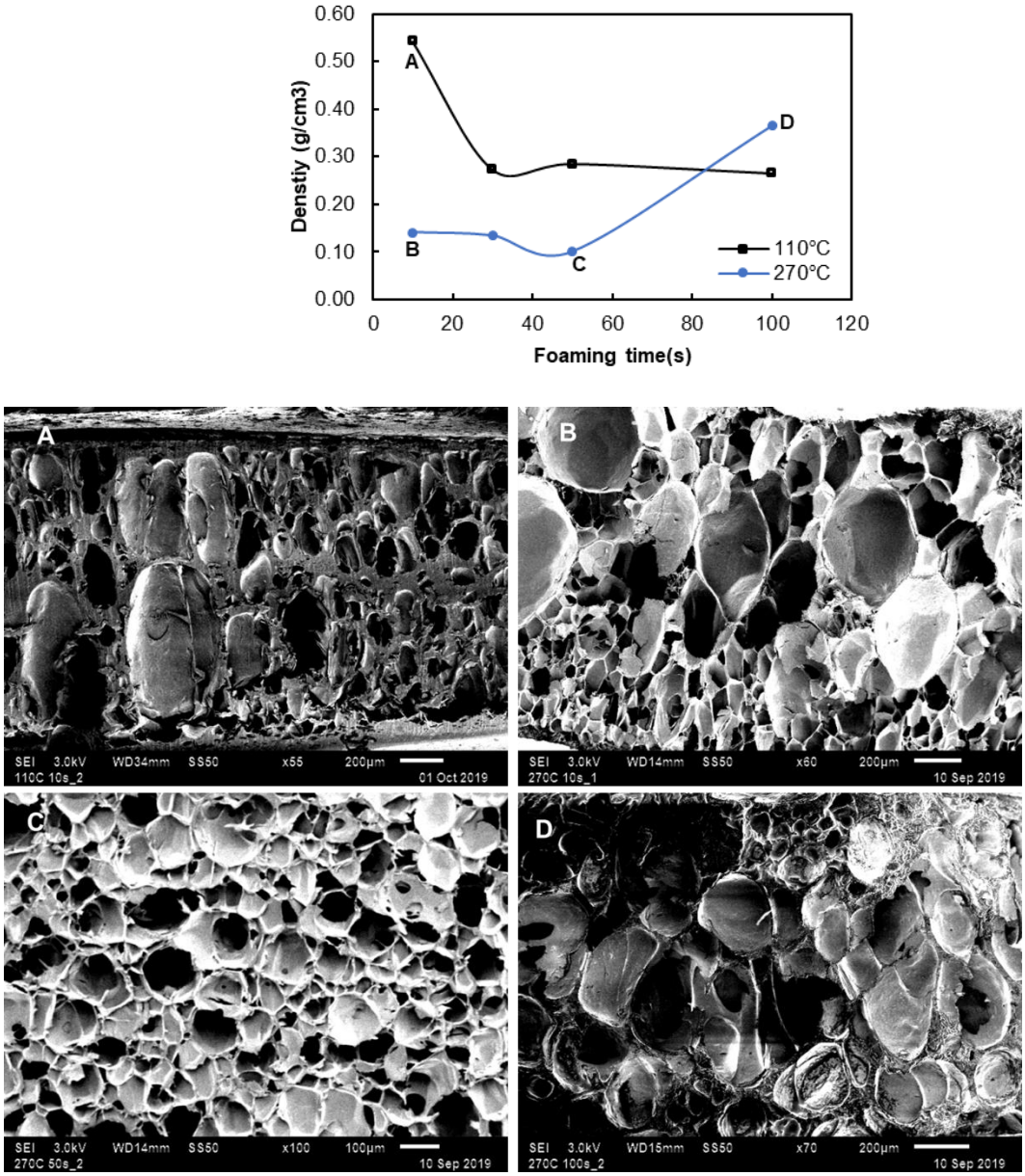

Figure 2.4. Above: density of 0.6mm samples with 110°C and 270°C but various foaming time; bottom: SEM images with same scale for 110°C 10s sample(image A), 270°C 10s sample(image B), 270°C 50s sample(image C) and 270°C 100s sample(image D)

2.3.4 Thermal Conductivity Measurements

There are a large number of cells filled with gas in the foams, and the thermal conductivity of the gas is much lower than that of the solid; therefore, foams exhibit excellent heat insulation performance.

Discs of the foams (0.5 inches in diameter) were sandwiched between two conducting copper cylinders, the top block whose temperatures is preheated to 50°C. whereas the bottom block was left at room temperature. Thermal contact between the copper cylinders and the samples was improved by applying glycerol. The whole system, i.e. the copper blocks and the foam sample were placed in a low-density insulation foam to ensure minimal heat loss. In this situation, the temperature change of the copper cylinders is entirely attributable to heat conduction through the foam and hence the thermal conductivity can be measured[75]. The experimental set-up has been sketched out in Figure 2.5 below.

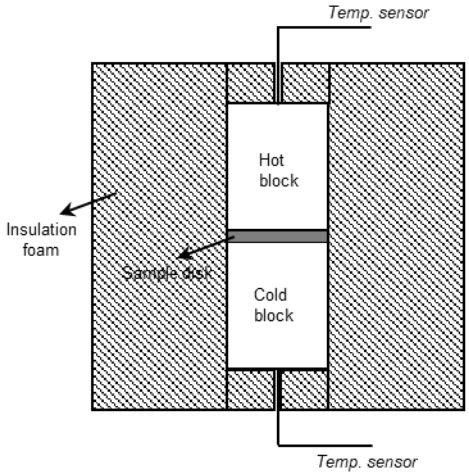

Figure 2.5. Schematic of the thermal conductivity measurements. Note that during measurements, the entire setup is encased in insulating foam to minimize heat loss to the environment.

We define the temperature difference to be:

$$q = T_2 - T_1 \qquad (1\text{-}1)$$

where T_2 is the temperature of hot block and T_1 is the temperature of cold one.

From:

$$m_c C_p \frac{d(T_2 - T_1)}{dt} = -2hS(T_2 - T_1) \qquad (1\text{-}2)$$

Where S is the contact area, m_c is the mass of copper block, C_p is the heat capacity of copper and h heat transfer coefficient ($h = \lambda / L$ and L is sample thickness). This gives

$$\frac{d\theta}{dt} = -\frac{2hS}{m_c C_p}\theta \qquad (1\text{-}3)$$

Integrated eq.(3) we can get:

$$\ln\theta = -\frac{2hS}{m_c C_p}t + \ln\theta_0 \qquad (1\text{-}4)$$

from which thermal conductivity λ can be calculated from the slope of eq.(1-4). A data sample of temperature changes with time for foam sample: 150°C, 30s, foam density: 0.133g/cm^3 is shown in Fig. 2.6A. Temperature difference changing with time with different foam densities is shown in Fig. 2.6B. The measured thermal conductivity values are shown in Fig. 2.7 below.

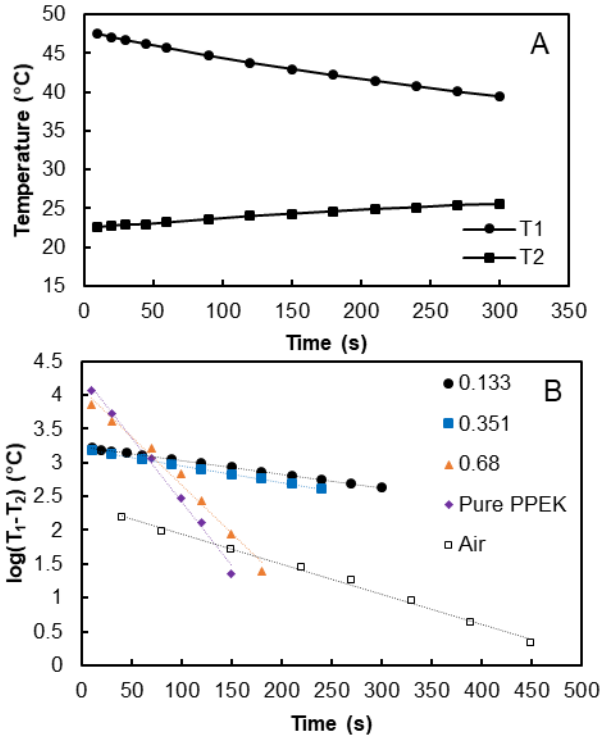

Figure 2.6. A: temperature changes with time for foam sample: 150°C, 30s, foam density: 0.133g/cm^3; B: temperature difference changing with time with different foam densities (units g/mL)

Gibson and Hilyard [78, 79] offer a simplified model to estimate polymeric foam thermal conductivity. The thermally conductive coefficient (λ) in their model is calculated according to the formula below:

$$\lambda=\lambda_s+\lambda_g+\lambda_r+\lambda_c \qquad (1\text{-}5)$$

where λ_s is the thermal conductivity of the solid, λ_g is the thermal conductivity of the gas in the foam cells (i.e. air in this case), λ_r is radiative heat transfer through the cell wall and the gas in the cells and λ_c is convective heat transfer of the gas in the cells. The main influencing

factors on the thermal conductivity of the foams are λ_s and λ_g. Thus, the equation above can be further simplified as the following format:

$$\lambda = \frac{2}{3}\frac{\rho}{\rho_s}\lambda_s + \left(1 - \frac{\rho}{\rho_s}\right)\lambda_{air} \qquad (1\text{-}6)$$

($\frac{2}{3}$ refers to the efficiency factor, $\frac{\rho}{\rho_s}$ refers to volume fraction, λ_s refers to the thermal conductivity of full dense solid). The thermal conductivity of the foams calculated with this model are also shown in figure 8 below.

From Fig. 2.7, it can be seen that thermal conductivity values from measurements are all higher the values get expected from the model. The low density foam has a measurement value as high as 0.135w/(m*K) may due to the nature of the PPEK polymer itself, i.e. pure PPEK has a measured thermal conductivity about 0.43w/(m*K), which is really a high value in polymeric system. To name but a few other polymers' thermal conductivities here for comparison: epoxy~0.17 w/(m*K); polysulfone ~0.25 w/(m*K); PVC~ 0.19 w/(m*K). [80]

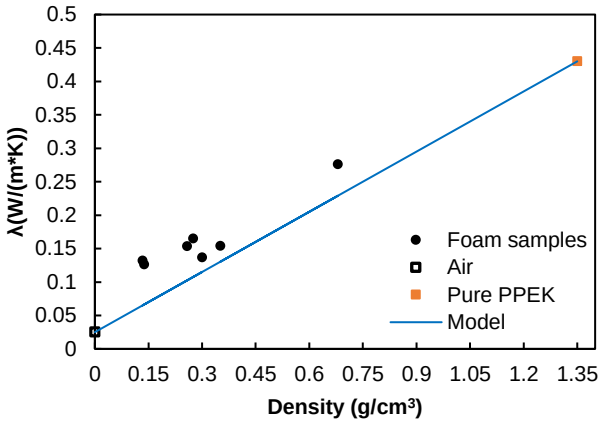

Figure 2.7. Foam thermal conductivities vs. foam densities

2.3.5 Indentation Tests of The Foams

Indentation tests were conducted with a TestResources testing machine. Foam samples were in the form of a round disk with the dimension of 12.7 mm in diameter and 3 mm in thickness. Indentation tests were conducted with 4 mm diameter ball-head indenter with a testing speed of 1 mm/min. The results of load vs. distance curve with various foam densities are shown below in Fig. 2.8. The threshold for the instrument to start recoding data is around 2.23N, and hence a portion of the data upon initial contact was not measured. Similar curves with load calculated from classical Hertz contact theory are also shown in figure 8 with eq. (1-7) and E^* as the fitting parameter. [81]

$$F = \frac{4}{3} E^* R^{1/2} h^{3/2} \qquad (1\text{-}7)$$

(R is the indenter radius and h is the depth of indentation and E^* is effective modulus)

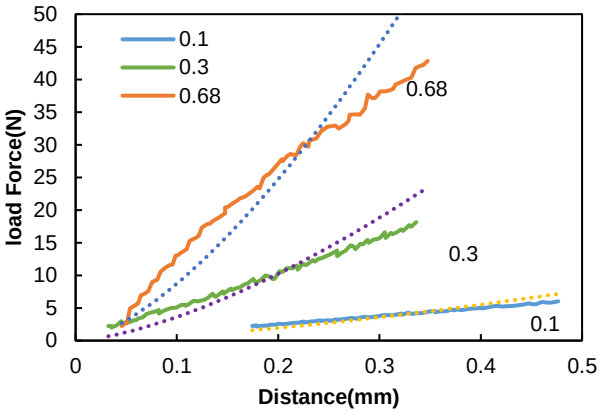

Figure 2. 8. Force Vs. distance curve of the indentation tests, dashed lines are fits to Eq. 8 of the foams with various densities listed in the legend (units g/mL).

Tests results show good reproducibility. For one sample disk, two runs would be conducted at two locations. An example of 0.373g/cm^3 sample is shown in Fig. 2.9.

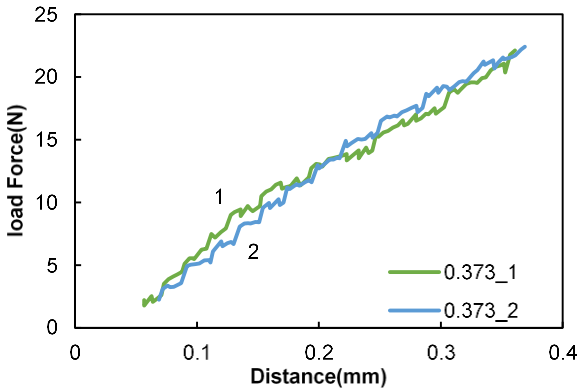

Figure 2.9. Sample reproducibility check with force Vs. distance curve for 0.373g/cm^3 sample.

The indentation tests proposed here is actually a "depth sensing indentation (DSI)" method, whose work based on elastic theory is proposed to describe contact area, given known indenter cross-sectional area with depth. DSI method is based on the theoretical work of Sneddon[82] and Oliver and Pharr's experimental approach[83], which is modified and proven by the later generation, for example, Jeremy L. et al. that can be effectively used in polymer system[84].

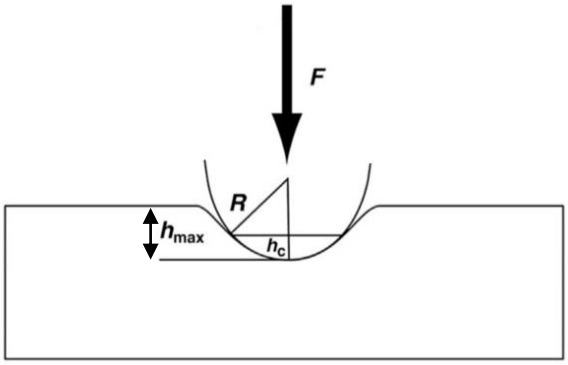

Figure 2. 10. Schematic of a DSI test. An indenter is pushed with force, *F*, into the surface an amount, *h*. A schematic for a spherical indenter is shown.

If the difference between the indenter modulus and sample modulus are greatly different, the sample's elastic modulus can be calculated as follows:

$$E = \frac{\left(1-\upsilon^2\right)\sqrt{\pi}}{2\sqrt{A}} \left.\frac{dF}{dh}\right|_{F_{\max}} \tag{1-8}$$

where υ is the Poisson ratio of the sample and A is the contace area.

The area–depth function depends on the shape of the indenter used and there are standard relationships for specific indenters. For a spherical indenter, contact area is:

$$A = \pi\left(2Rh_c + h_c^{\,2}\right) \tag{1-9}$$

where *R* is the indenter radius.

There are corrections made for the depth, *h*, to become h_C to account for the actual contact area since *A* is less than what would be calculated for *h* (see Figure 2.10) and h_C is found with the following equation:

$$h_c = h_{\max} - \varepsilon \cdot \frac{F_{\max}}{\partial F / \partial h} \tag{1-10}$$

where ε is a correction factor based on tip shape (ε = 0.75 for a sphere) . The values of the foam modulus *E* are calculated and shown in the following Fig. 2.11.

It's worth mentioning that, foam modulus calculated with best fit E^* value from figure 10 above for the 0.1g/cm^3, 0.3g/cm^3 and 0.68 g/cm^3 samples are also shown in figure 12 below. As it can be seen that the Hertz theory's modulus is lower than DSI method for low density foams (0.1 g/cm^3 and 0.3 g/cm^3 ones) but higher than DSI method for high density foam(0.68 g/cm^3).

Gibson et al. gives a model simplified from finite element analysis to predict the closed cell polymeric foam modulus as well. [79] The main equation used in the model is as follows:

$$\frac{E}{E_s} = 0.32\left[\left(\frac{\rho}{\rho_s}\right)^2 + \left(\frac{\rho}{\rho_s}\right)\right] \tag{1-11}$$

E refers to foam modulus, ρ refers to foam density and subscript s refers to corresponding quantity of the pure polymer. The foam modulus from this model are also shown in Fig. 2.11. The modulus of the model shows reasonable agreement with the experimental results with low foam density (<0.4g/cm^3). However, when density goes higher, the model greatly overestimates the experiments.

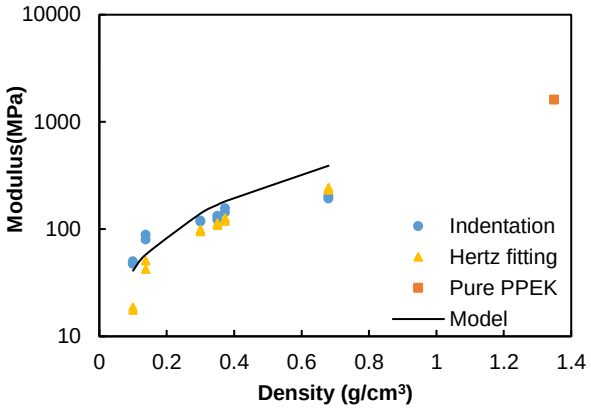

Figure 2. 11. Foam modulus vs. foam density in log scale

2.3.6 Test of Foam's Temperature Stability

For a foam to be useful as a high temperature insulator or for structural applications, it is critical to verify that it remains intact (i.e. does not collapse) even after a long period at high temperature. A preliminary test of high temperature stability was conducted. A foam was been prepared at a foaming temperature of 150°C and 30s of foaming time (Fig.2.12A). It was heated at 200°C for 2 hours (Fig. 2.12B). From the images, it can be seen that the two images appear very similar, i.e. there is no evidence of cell coalescence or collapse in this time. Also, the density of the foam is almost the same before and after treatment, i.e.0.14g/cm^3.

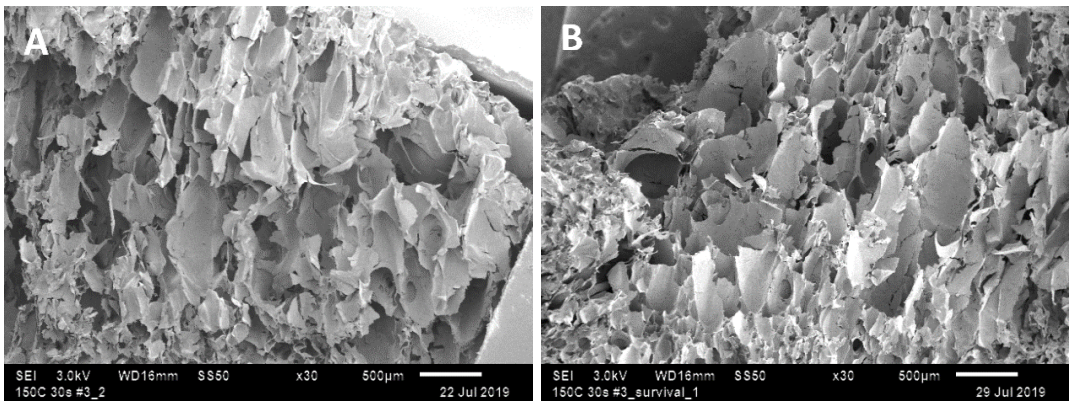

Figure 2.12. Foam survival test: A: SEM image of the cross-section of the foam prepared under 150°C 30s ; B:same foam after heated under 200°C for 2 hours

2.4 Conclusion

A method of producing PPEK foam has been developed. The method consists of swelling the polymer with a solvent (dichloromethane), and heating it to nucleate foam bubbles in a one-step batch foaming process, followed by cooling to vitrify the polymer. Microcellular PPEK foams with the cell diameter of only few tens of microns can be prepared. Foam density ranged from 0.1g/cm^3 to 0.68g/cm^3, correlating a density reduction of 50-93%.

The thermal conductivity of the foams is low, i.e. less than 0.2 W/(m*K) for the low-density ones. Thermal conductivity values from measurements are all higher the values get expected from the model. This may due to the nature of the PPEK polymer itself, i.e. pure PPEK has a measured thermal conductivity about 0.43w/(m*K), which is really a high value in polymeric system. The stability of the foam has been tested with a survival test, which shows that the continuous working temperature of the foam are very likely to exceed 200°C.

The mechanical properties of such foams have also been characterized and studied with indentation tests.

Due to the thermal and mechanical behavior of the PPEK foams, they may find applications as high temperature structural materials or high temperature thermal or electrical insulation.

3.0 Compression-induced Fold Localization of Thin Films Bonded to Viscous Substrate

3.1 Introduction

When a thin elastic film floating on a liquid support in gravity is compressed uniaxially, it buckles to form uniform, roughly sinusoidal, wrinkles. Upon further compression, one of the wrinkles evolves to have a larger amplitude whereas the remaining wrinkles diminish. This localization of curvature is called the wrinkle-to-fold transition[9].

The substrate of the previous paragraph can be regarded as "energy-conserving" substrate in the sense that the substrate deformation needed to accommodate the film buckling can be described in terms of a potential energy contribution to the total system energy. Minimization of the total system energy can then capture both the initial wrinkle profiles as well as the profiles of the localized folds.

In a recent article our group showed that an entirely different situation – an elastic film bonded to a viscous substrate – also shows fold localization[85]. Unlike the cases of the previous paragraph, viscous supports are not energy-conserving, but instead fully dissipate mechanical energy. Thus approaches based on energy conservation are not applicable; one must inherently deal with the rate at which instabilities develop[11]. To our knowledge, our previous research is the only article published thus far that mentions fold localization of elastic films on viscous substrates[85]. Virtually all of that previous article was focused on developing a detailed model of wrinkling of elastic films on viscous supports. The issue of fold localization was mentioned only briefly and qualitatively. The goal of this research is to describe in greater detail the experimental observations of the buckling of thin elastic films floating on dissipative substrates. While a theoretical description of this phenomenon remains

incomplete, the observations described here go a long way towards pinning down the key experimental aspects and identifying some of the relevant physics.

The experimental situation for this project is as follows (see Fig. 3.1 for the sketch of the experimental set-up). The viscous liquid is layered on a prestretched rubber substrate, and a strip of film is then placed on the surface of the liquid. Releasing the rubber substrate at a well-controlled rate imposes compressive stress on the liquid, which in turn compresses the film and induces buckling at the free surface.

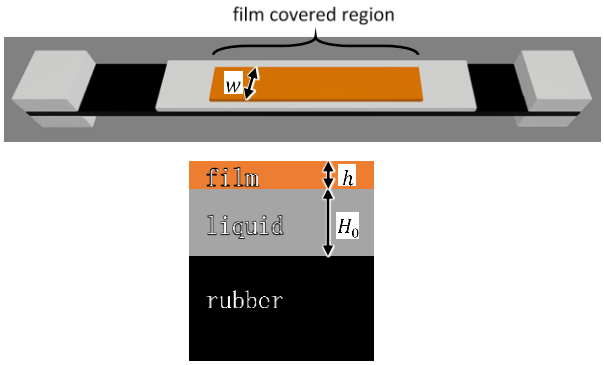

Figure 3.1. Schematic of the experiment. (Note that the actual experimental setup, and especially the clamps, are significantly more complex than noted here.)

Here, we assume the film to be a thin elastic plate. The analysis is similar to that of Huang and Suo[13] who studied wrinkling of a pre-compressed film on a viscous layer. However, it differs from Huang and Suo in two ways. First, the lower surface of the viscous layer is not stationary in the present case, but instead subject to a specified strain rate due to contraction of the rubber sheet. Second, the film does not bear a prestress; instead, the compressive stress in the film develops with time. Thus, the buckling instability is driven not by relaxation of the pre-stressed film, but by the viscous stresses transferred from the contracting rubber sheet to the film via the liquid layer. An analytical shear-lag model was used in our previous work [85] to predict the evolution of the compressive stress profile in the film prior to buckling.

We will now discuss the reason for applying the compression as described in Fig.3.2. At first glance, it may seem that the floating film may be compressed simply by pushing its ends together, as was done by Pocivacsek et al[9]. This is conceptually equivalent to compressing a surface film in a Langmuir trough. However, since the substrate is dissipative, such a situation is likely to give localized buckling near the ends. Indeed we showed previously that prior to buckling, the in-plane displacement field in the film spreads diffusively.[85] Thus, for a sufficiently large system size, the film far from the compressed ends is guaranteed to stay stress-free while the film near the ends compresses sufficiently to buckle. Clearly, such end-compression cannot give homogeneous strain for a sufficiently large film; such experiments would necessarily be affected by the system size.

One simple approach that can compress the film uniformly is to exploit thermal mismatch. An exemplary case was of Vandeparre et al.[86], who spincoated polystyrene (50-1000 nm thick) onto silicon wafers, followed by thermal evaporation of titanium (10 or 20 nm) onto the polystyrene surface. Heating this system caused two changes. First, due to differential thermal expansion (the silicon wafer expanded less than the titanium layer), a strain mismatch was created such that the metal layer experienced compression. Second, the polystyrene layer exceeded its glass transition temperature and hence became capable of flow. The titanium film then gradually developed wrinkles which relaxed the thermally-generated compressive stress. One limitation of this approach is that with a mismatch in thermal expansion coefficient, strains exceeding roughly 1% are difficult to realize, and indeed in Vandeparre et al, the strain mismatch was only roughly 0.05%. Similar research was conducted even earlier by Yoo et al[87].

Hobart et al[12] and the subsequent analyses by Suo[88] examine situations with a somewhat different cause of compressive stress. In those cases, the film bears compressive

stress because it is deposited hetroepitaxially onto another substrate. Such strains also tend to be small.

Since the rubber layer can be prestretched by many ten percent (sometimes even few hundred percent), the chief advantages of this method over alternate approaches[16, 89] are that a large strain can be imposed large strains can be applied, and the film experiences uniform compression over nearly its entire surface. Furthermore, the rate of release can be controlled directly – this is critical since viscous stresses depend on the rate. Finally, unlike the end-compression approach[9], if the substrate release rate is sufficiently large, almost the entire film experiences the same uniform compression. Thus with sufficiently long films, infinite film conditions may be approximated.

Early during this project, several crude experiments were conducted, and they show that the process can be rather complex. This can be illustrated by Fig. 3.2. Fig. 3.2A shows a rubber-liquid-film sample with prestretched rubber, which is then released rapidly. Fig. 3.2B shows that the entire three-layer sample undergoes global bending. This is not surprising and is attributable to the mismatch between the tensile stress in the rubber and the compressive stress in the film. This effect can be reduced by maintaining sufficient tension in the rubber strip during the entire process. Fig. 3.2C&D shows an experiment conducted "by hand" to illustrate the effect of film width. Two strips of film were floated onto a thin layer of viscous fluid placed on a single strip of rubber. The strip was stretched and released rapidly. At short times during or after compression, the both samples behave similarly – not surprising since they experience the same strain and strain rate. However, for the narrow film, the liquid layer rapidly recedes inwards under the peaks of the buckles, thus allowing sharp folds to become substantially wider. The same happens for the wider film, but takes a longer time.

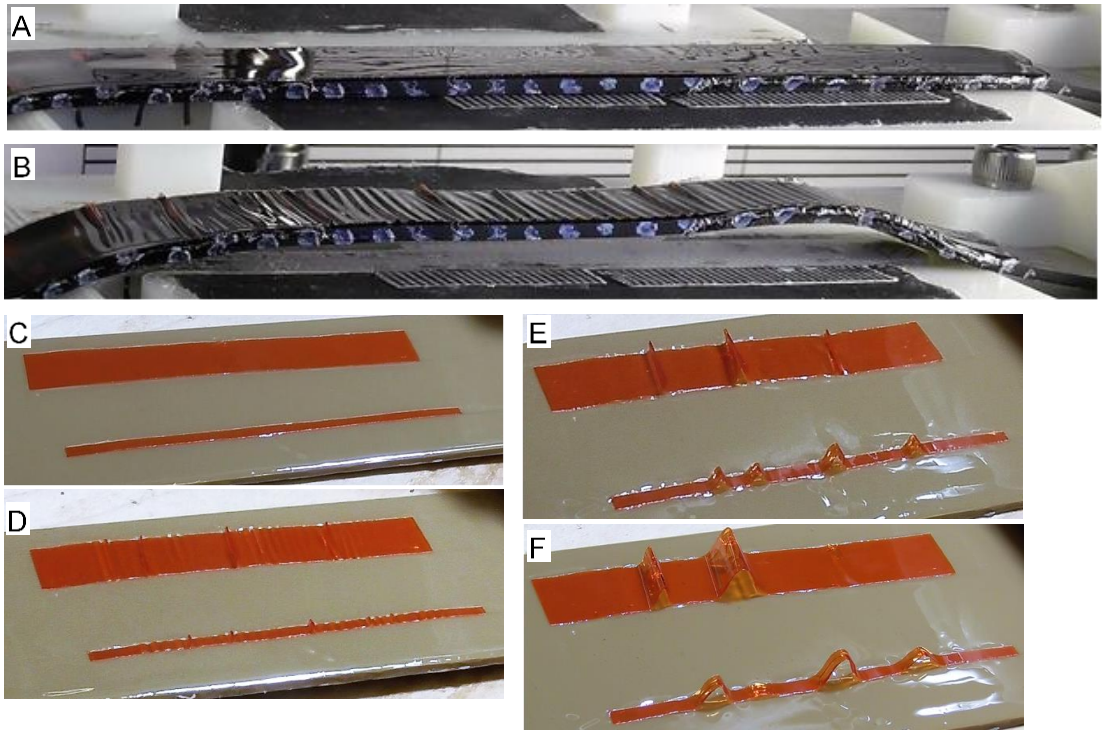

Figure 3.2. Snapshots from hand videos (A&B) showing global bending upon releasing the sample, and (C-F) air entering under folds.

Several such crude experiments were conducted, and these experiments guided us in formulating some key questions: (1) Does fold localization require a certain minimum strain? Or can sinusoidal wrinkles evolve to localized folds at arbitrarily small amplitude? (2) Does the long edge of the film play a role in initiating the wrinkle-to-fold transition, analogous to how buckle delamination of films off substrates often starts at edges? Or can edge effects be neglected, effectively regarding the situation as a 2D problem? (3) Is fold localization favored or suppressed by increasing the two main parameters, liquid layer thickness and strain rate? (4) Is the wrinkling process or the fold localization sensitive to small flaws?

This project is a collaborative work with other students (Eshwar Hamesh and Anantha Padmanabha Sarma). My contribution to this work is as follows: (1) design and set up the experimental equipment including the multi-angle video recording; (2) develop the digital image correlation analysis approach for video data processing; (3) devising the methods of

sample preparation; (4) run preliminary tests for the project ; (5) analysis of the effect of rate and liquid layer thickness to the system, i.e. address item (3) in last paragraph.

3.2 Experimental Section

Samples consist of butyl rubber strips of 1.58 mm thickness that are cut to a width of either 1 inch (25.4 mm) or 0.5 inch (12.7 mm). The liquid used is BASF Oppanol B15 (polyisobutylene).

The liquid used here is polyisobutylene of molecular weight (MW) of roughly 85 kg/mol. The rheological characteristics of this fluid are shown in Fig.15. The complex viscosity, η, at low frequency is roughly 10^6 Pa.s, with modest shear thinning. The viscosity of the fluid used in this project is about 1000 times higher than our previous work (polyisoprene, MW: 46 kg mol^{-1}; η =1170 Pa·s).[85] The reasons for using higher viscosity fluid are as follows: (1) due to the limitation of the shear lag model, the ends of the film are free from stress. Therefore the ends of the films do not develop sufficient stress to buckle. Moreover, from the diffusion time scale of the shear lag solution:

$$\tau = \frac{4L^2}{\pi^2 h H_0} \frac{\eta\left(1-\nu^2\right)}{E} \tag{3-1}$$

lower viscosity reduces τ and lead to the limitation that wrinkling appear at $t < \tau$ hard to access. Shear lag solution is the solution of the shear lag model, which is developed to predict evolution of compressive stress in the elastic film. Thus, high viscosity fluid could lead to a larger time scale τ, in which case, even within a short time, i.e. $t < \tau$, the stress developed within the film would more likely to be uniform, in which case a panorama wrinkling pattern with uniform wrinkling state could be achieved, even with the “end regions” of the film. Also, higher viscosity makes τ larger, which may feasible to observe and capture the

formation of wrinkles and the critical strain value for wrinkle formation can be studied. (2) High viscosity fluid favors sample preparation process, i.e. samples with targeted liquid layer thickness can be well prepared. For example, using platen press to compress down the sample with target thickness spacers for preparing samples. This is hard to achieve for low viscosity since the liquid are likely to flow, which may lead to the not-uniformity of the liquid layer thickness. Therefore, the wrinkling and folding phenomena that happens after releasing of the rubber can be better captured and studied with higher viscosity fluid.

In most of the experiments, the rates applied are on the order of 0.01 s^{-1} and shear thinning effects, although present, may be modest. The highest rates in our experiments are roughly 0.09 s^{-1} and shear thinning may be somewhat significant for these experiments. The fluid is also viscoelastic as judged by the significant magnitude of the storage modulus G' as compared to the loss modulus G". At the conditions typical of most of the experiments (rates on the order of 0.01 s^{-1} and strains of a few percent), we may estimate the stress contributions as follows: The fluid stresses attributable to viscous forces are on the order of $(\text{viscosity}) \times (\text{rate}) \sim 10^6 \times 0.01 \sim 10^4$ Pa. The stresses attributable to elastic forces are on the order of $(\text{modulus}) \times (\text{strain}) \sim 10^4 \times 0.05 \sim 500$ Pa. This suggests that most of the phenomena are due to viscosity, and hence a purely viscous Newtonian fluid would show the same phenomena, at least qualitatively.

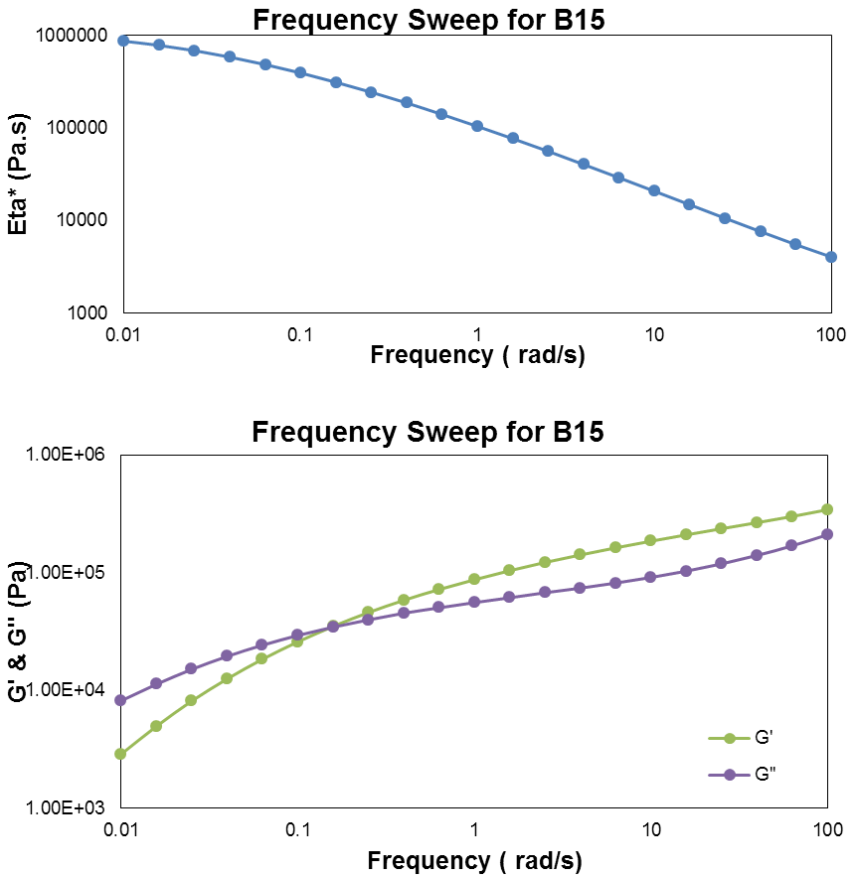

Figure 3.3. Dynamic oscillatory rheology of the fluid B15 used in this research

The films used in the experiments were polyester shimstock films purchased from McMaster-Carr with thicknesses in the range of 0.0005 inches to 0.002 inches (i.e. 12.7 micron to 50 micron). Most of the experiments used a film thickness of 25 micron.

Samples were prepared by rolling a long cylinder of polyisobutylene of the desired mass and length and placing it on the rubber strip, typically 130 mm long. It was then covered with a sheet of PTFE, pressed in a compression molding machine with the desired spacers to regulate the final compressed thickness, and the PTFE cover layer was removed. In some later experiments, a sheet of silicone rubber was found to be more convenient than a PTFE sheet.

Fig. 3.1 consists of clamping the rubber strip, already covered with the liquid layer, between grips which slide on a rail assembly. The grips can be translated up to 50 mm at speeds of up to 8 mm/s using linear stepper motor actuators (Zaber T-NA08A50). The rubber strip was stretched to about 130% of its original length. The film was then applied on the liquid surface taking care to avoid air pockets. The rubber strip was then allowed to recover at the desired rate, to typically 122% of its original length. Some later experiments used a greater prestretch and a greater extent of recovery. The stain rate range in the experiments are roughly on the order of 0.001 s^{-1} to 0.09 s^{-1}.

The film is visualized at three different magnifications using three cameras simultaneously. Visualization of fold localization is somewhat complicated by the fact that the location of the fold is unpredictable, and the film compression is usually too short to allow adjusting the camera position. Moreover, the folds are often well-spaced and hence the highest magnification camera would often see one or no folds. Therefore, all the videos and most of the figures in this chapter show only the intermediate magnification which conclusively shows that folds appear, but cannot resolve the width of the fold.

The camera-facing edge of the rubber strip was marked with white ink spots, and digital image correlation (DIC) analysis using the Blender software was used to extract the displacement of these spots with time. Fig. 3.4 below shows an example of calculating strain data from images. Right column in the figure shows sequence of images with the lowest image being the prestretched state. Top left figure shows the displacement of each marker vs its original position. Slope of these data gives the strain at that instant, which is shown in the bottom left figure. With this DIC analysis, the information of local strain in the rubber stripe can be obtained.

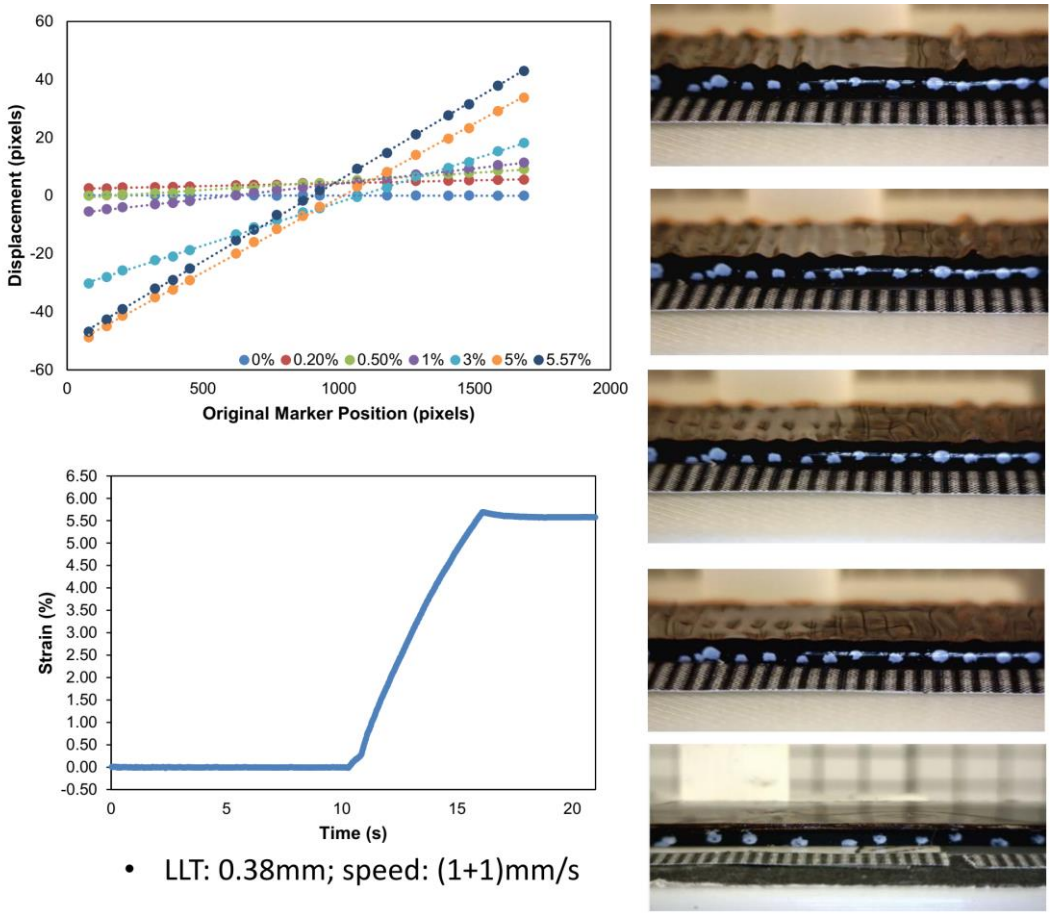

Figure 3.4. Calculation of strain data from images. Right column shows sequence of images with the lowest image being the prestretched state. Top left shows the displacement of each marker vs its original position. Slope of these data gives the strain at that instant, bottom left.

3.3 Result and Discussion

3.3.1 Imposed vs. Actual Strain

In the experimental setup, the local strain within the sample cannot be controlled directly. It is possible to only control the speed of the grips that permit retraction of the rubber. Since the portion of the sample that bears the film is effectively stiffer than the exposed portion, one may expect that the end-displacement is accommodated unequally over

the length of the sample. To quantify this, Fig. 3.5 shows the strain obtained from three experiments which differ only in the thickness of the polyester film. In all three cases, each the experiment was conducted twice: once with the rubber strip covered with the liquid layer, and once with further addition of the polyester film. The dotted lines in Fig. 3.5 show that in the absence of the polyester films, the rubber strips experience nearly uniform deformation rate with time as judged by the slope of the strain-time data. When the film is applied to the liquid surface however, the deformation occurs in two distinct stages, a first slow deformation, followed by a sharp increase in rate to nearly the value realized in the absence of the film. Since the strain in the film-covered region is less than the expected value, one must expect the strain in the remainder of the rubber (i.e. the regions near the clamps) to be correspondingly higher. Indeed Fig. Appendix B.1 confirms that the strain in the rubber strip is higher near the grips as compared to the middle of the film-covered region.

This behavior may be readily explained as follows. Prior to buckling the film resists compression by in-plane stress; the effective stiffness of the film is high and hence the strain remains low. Subsequent to buckling, the film resists compression by bending. Since the effective stiffness of any slender body is much lower post-buckling than when it is flat, the rate increases sharply.

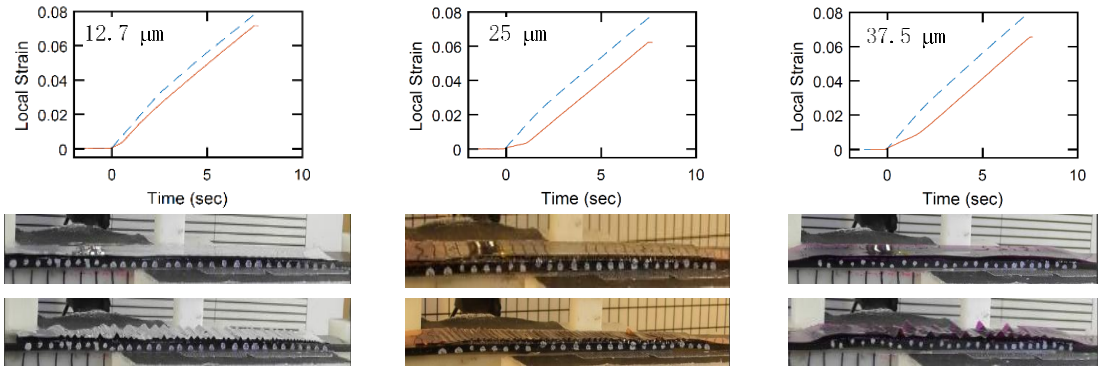

Figure 3.5. Strain vs time films with the thickness noted at the top left of each graph. In each graph, the dashed blue line represents the liquid-on-rubber samples, whereas solid orange lines indicate film-on-liquid-on-rubber samples. The images are snapshots from the videos taken before and immediately after the elbow in the strain vs. time graph.

3.3.2 Effect of Sample Width

The experiments of the previous section were conducted using rubber strips that were 12.7 mm wide under relaxed conditions. The prestretch imposed during the experiment caused the rubber strip to become narrower (roughly 11 mm wide is expected for uniaxial elongation), and the film was cut to roughly the same width. At least judging visually, the film, the liquid layer, and the rubber strip all had the same width. One key question is whether the behavior is sensitive to film width or to the presence of the edge of the film. If effects of film width prove to be negligible, the situation may be analyzed with a 2D approximation which would be a major theoretical simplification. To test this, experiments were conducted where the polyester film width was varied while keeping the rubber strip (and the width of the liquid layer) fixed. Fig. 3.6 shows the results, all with a liquid layer thickness of 0.3 mm. Films of width 3 mm, 6 mm, and 8 mm (Fig. 3.6B,C,D) show roughly

comparable behavior with wrinkles developing at small strain, followed by fold localization. The behavior at 1 mm width (Fig. 3.6A) is quite different: as the wrinkles grow in amplitude, the film delaminates off the liquid which may be regarded as interfacial/adhesive failure at the film/liquid interface. Visually at least, this appears similar to the delamination from a winkled state for a film bonded to a soft solid substrate[90]. If the fluid has a much lower viscosity, Fig. 3.6C-F already showed that for narrow films, air invades under the peaks of the wrinkles. Although this can sometimes visually resemble delamination, it is not true delamination, i.e. there is no separation of the film from the fluid, instead the fluid remains attached to the film (as well as to the rubber substrate).

Both of these behaviors of narrow films have a common cause which can be understood as follows. Fold localization implies a high curvature, which imposes a large elastic energy penalty. One way to reduce this curvature is to simply widen the fold, but this requires increasing the volume under the fold. Delamination and fluid flow are the two ways whereby the surrounding medium (air in this case) can occupy the space under the folds, thus allowing them to become wider. For wide samples, both these mechanisms are slowed down, thus allowing the behavior to become nearly independent of edge effects.

Finally, Fig. 3.6E shows the situation when the rubber substrate, the liquid layer, and the film are all cut to the same width. This experiment showed wrinkles and folds that were much less regular. Moreover, unlike Fig. 3.6A-D where wrinkles and folds spanned the entire width of the sample, such samples often showed a pair of antisymmetric folds.

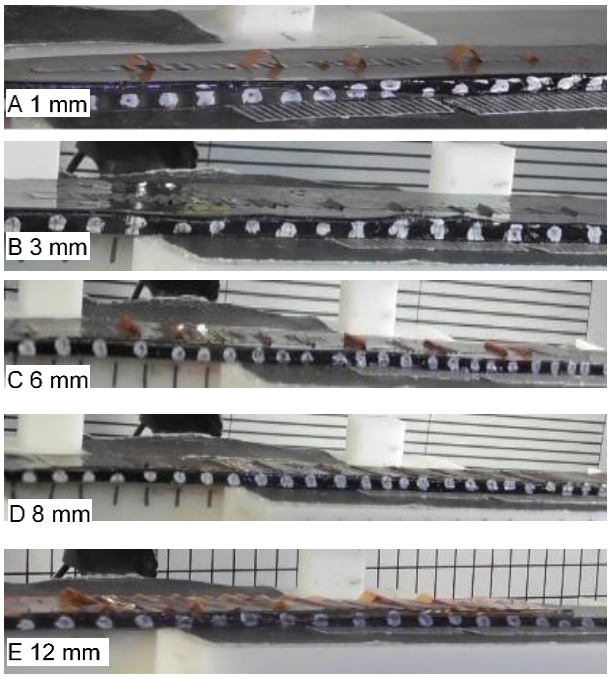

Figure 3.6. Effect of film width on fold localization. The last example has width of ~25 mm. In all the remaining cases, the relaxed rubber width is 12.7 mm, and the film width is as noted in each figure.

In summary, the effects of sample width are much more complex than recognized in our previous research. For very narrow film widths, the edge allows at least two kinds of failure. One resembles true delamination off a solid substrate. Since this requires violating the no slip boundary condition at the film-liquid interface, we speculate that it is only possible if the liquid is viscoelastic. In the other, the liquid/air interface recedes inwards, thus allowing air to invade the space under the peaks of the buckles. Finally, the sample edge may contribute imperfections that affect the buckling process. For this reason, all subsequent experiments use a film width of 8 mm, whereas the rubber and the B15 liquid are both significantly wider. For all practical purposes, the situation may therefore be regarded as a strip of film floating on a sea of fluid.

3.3.3 Effect of Rate and Liquid Layer Thickness

We examine the effect of strain rate as illustrated in Fig. 3.7, where the translation speed of the grips was either 0.1 mm/s (Fig. 3.7A) or 6 mm/s (Fig. 3.7B). At the low rate, folds appear readily during the loading process and, folds suppress the growth of neighboring wrinkles. At the high rate, there is no significant localization during the loading process. Images were also recorded after the loading was completed to record the evolution of the buckled structure under quiescent conditions. In Fig. 3.7A, the well-developed folds further evolved over several minutes so that some of the folds became even taller, whereas other folds or wrinkles reverted to a nearly flat state. In Fig. 3.7B, the film showed only modest localization at the end of the loading process. However, within less than a minute, some of the wrinkles flattened significantly whereas others localized to a high curvature. It is interesting to note that in Fig. 3.7B that localization is not an irreversible process; a localized fold first forms on the far left (5 min image), but eventually loses amplitude to a neighboring fold (23 min image).

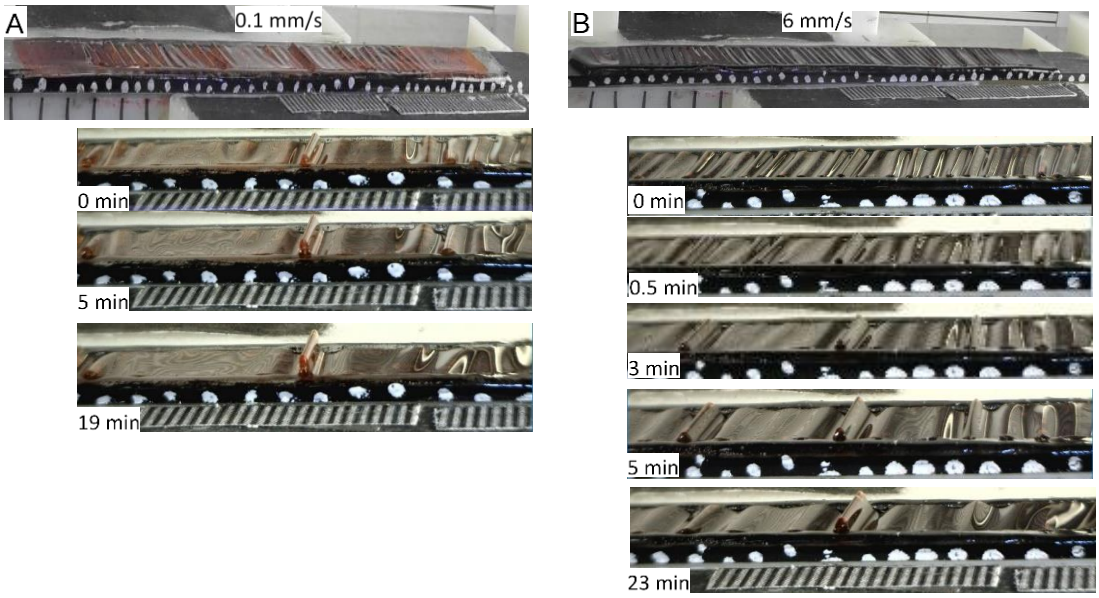

Figure 3.7. Effect of loading rate. The speed listed in the upper two images is the translation speed of each grip. The lower set of images were taken after the loading was completed to illustrate evolution of the film with time. For low speed loading (A) folds appear during loading and sharpen after loading is complete. For high speed loading (B) folds localize after loading is complete. Note that in the lower right set of images that between 5 and 25 min, the leftmost fold relaxes, whereas the central one grows.

In the experiments of Fig. 3.1, the thickness of the liquid layer is 0.38 mm. Fig. 3.8 compares this case against three other liquid layer thickness, all compared at a fixed rate. This shows that fold localization is acutely sensitive to liquid layer thickness. At small liquid layer thickness, localized folds appear early during the folding process at somewhat regular spacing. Similar to Fig. 3.8, once a fold appears, it rapidly relaxes the wrinkles in its vicinity. At the highest liquid thickness, there is no significant fold localization up to the end of the loading process.

Once again, the latter case, when the sample was allowed to rest after loading, folds appeared at some locations whereas the remaining film reverted back to flatness.

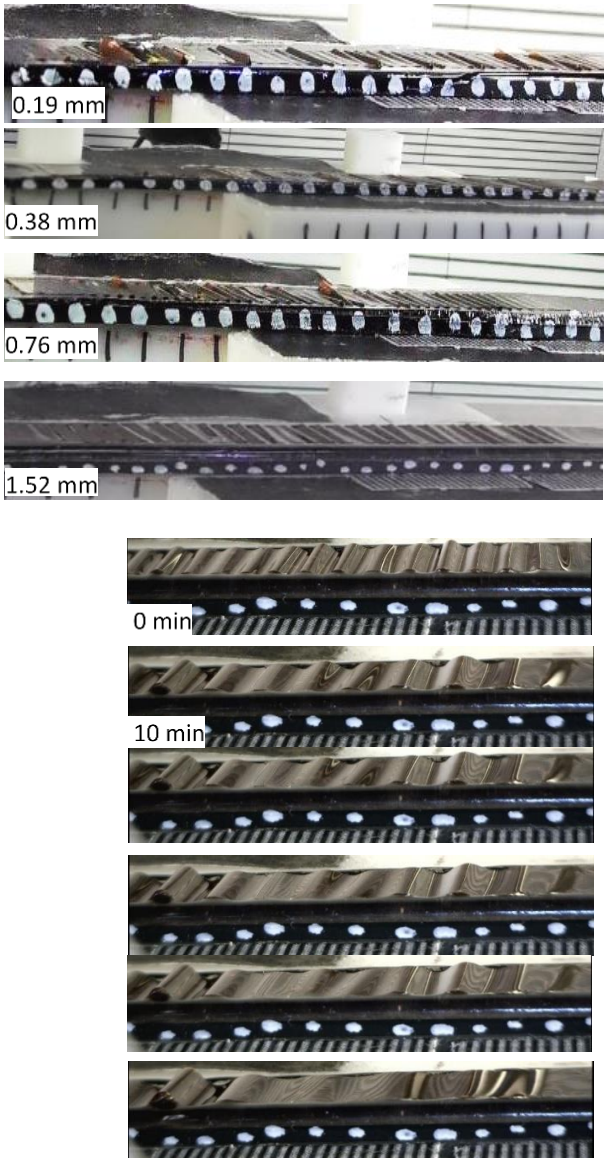

Figure 3.8. Effect of liquid layer thickness on fold localization. Left four images show that increasing liquid layer thickness reduces fold localization. RHS set of images are a time sequence at the liquid layer thickness of 1.52 mm after loading is complete to show that wrinkles transiton into localized folds. Note than between 16 and 35 minues, the wrinkles towards the right relax and the fold on the left grows.

3.4 Conclusion

In brief, the central experimental observations here is as follows: (1) For a short duration at the beginning of the experiment, the strain rate is lower than most of the latter

portion of the experiment. Once buckling is initiated, the strain rate is nearly constant with time and can be controlled precisely by varying the translational speed of the clamps. (2) The effects of sample width are complicated. For very narrow film widths, the edge allows at least two kinds of failure. One resembles true delamination off a solid substrate. In the other, the liquid/air interface recedes inwards, thus allowing air to invade the space under the peaks of the buckles. Finally, the sample edge may contribute imperfections that affect the buckling process. (3) Folding appears at low rate and low liquid thickness. However, developing folds requires long time. Thus, under rapid loading, multiple wrinkles or folds may appear.

The paper work of this project now is still under organizing and summarizing. Also, some additional work still needs to be done: (1) Try to pin-down the certain minimum strain needed for showing folding localization. (2) Better understanding the role of the long edge of the film in the wrinkling folding process. (3) Better understanding the sensitiveness to small flaws of the wrinkling process or the fold localization.

4.0 Stretching-induced Wrinkling in Plastic-rubber Composites

4.1 Background

A thin stiff elastic film bonded to a softer elastic substrate can buckle to form wrinkle patterns when subjected to compressive stress. The past decade has seen numerous articles in this area exploring the fundamental mechanics of such buckling[1-4], and applications such as smart surfaces with tunable adhesion, friction, and wettability, flexible electronics, thin film metrology[91-94]. A large majority of research has examined elastic systems, i.e. the thin film as well as the soft substrate were treated as elastic (often linearly elastic) materials[1, 3, 5, 6]. But materials used in experiments or of interest to practical applications have more complex material properties, and there is now a growing literature on thin film wrinkling when the substrate or film is an inviscid liquid[7-9], viscous liquid[10-12], viscoelastic[14-16], or capable of yielding[17, 18]. It is in this spirit that the current project examines the deformation and wrinkling behavior of films comprising a hyperelastic rubber and yielding plastic sheets bonded to each other[95, 96].

The essential idea, illustrated schematically in Fig.4.1A, appears in a previous patent[95]. Fig. 4.1B shows a trilayer film composed of a styrene-ethylene/propylene-styrene (SEPS) rubber sheet of 860 micron thickness bonded to two face layers of linear low density polyethylene (LLDPE), each 50 micron thick. This sample was then stretched to a nominal strain of 200%, and released, upon which the surface develops strong permanent wrinkles (Fig. 4.1C&D). Fig. 1E shows the wrinkle pattern replicated in silicone rubber (details in the experimental section below). The mechanics underlying this stretch-release-induced wrinkling have been previously explained as follows[95]: the LLDPE polymer comprising the face layers is known to undergo irreversible plastic deformation upon stretching. In

contrast, the SEPS elastomer in the mid-layer stretches reversibly. Thus, upon stretching, a large strain mismatch is created: the stress-free length of the face layers is longer (roughly by two-fold) than the stress-free length of the elastomer. Thus upon releasing, the elastomer imposes a compressive stress on the face layers. Being much thinner and stiffer than the elastomer, these face layers then buckle into a wrinkle pattern. In the simplest interpretation[96], the situation immediately prior to release is analogous to the numerous citations in the first paragraph: a longer stiffer elastic film, bonded to a shorter, softer substrate. Thus, upon release wrinkles appear due to a competition between the elastic energy of bending the film vs the elastic energy of deforming the rubber.

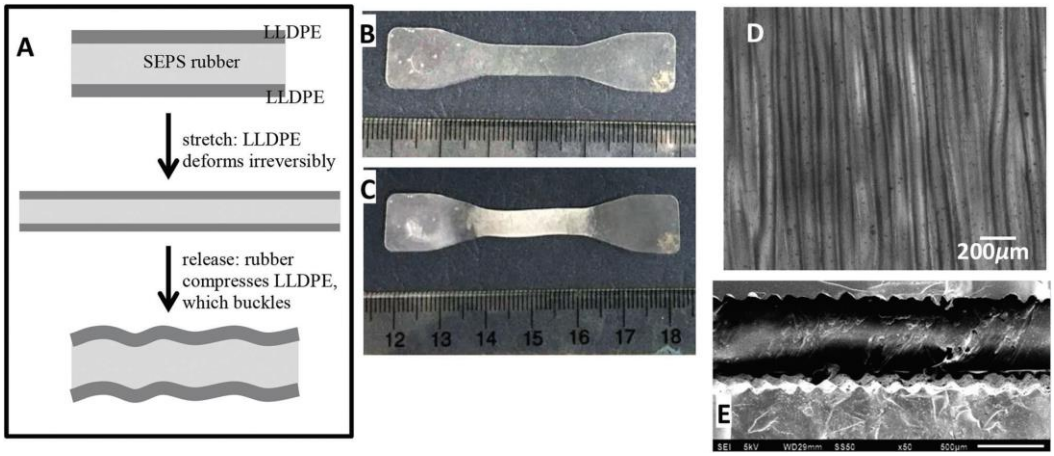

Figure 4.1 (A) Schematic representation of the experiment; images of (B) a sample before stretching, and (C) the same sample after stretching; (D) an optical microscope image of the wrinkled surface; (E) SEM image of the cross sectional profile of the sample replicated in silicone rubber.

The idea of using stretching of a plastic-elastic composite to create strain mismatch appears to be generalizable to many different plastics, and the patent by Kreuger[95] cited examples of numerous pairs of elastomers and polyolefin plastic face layers that gave similar results. Later Hu et al.[96] conducted elegant experiments of stretching-induced wrinkles, except that in their case, the thin plastic layer (polypropylene, PP) was sandwiched between two thick elastomer face layers (SEPS). Hu et al.[96] also developed a model for the buckling

process and for the wavelength of the buckles. However the model had significant deficiencies. First, it ignored the fact that the plastic layer at the end of stretching must be much thinner than the original thickness; if the correct thickness were used, the model predictions would strongly differ from experiments in that same paper. Second, all materials were treated as being elastic during release; plasticity was deemed only important in that the stretching induced a strain mismatch. In fact this article will point out that film plasticity plays a dominant role at all stages: stretching, recovery prior to buckling, and post-buckling.

4.2 Experimental Section

The rubber used was G1730 SEPS triblock copolymer containing 22% polystyrene. The manufacturer's datasheet quotes an ultimate elongation of 880%, a Shore A hardness of 60. Uniaxial elongation tests of dogbone samples gave a modulus of roughly 3.3 MPa. The LLDPE films were commercial films (Mitsui HC-50) marketed for food-packaging applications with a thickness of 50 micron quoted by the manufacturer.

The LLDPE films retain some residual stress from the manufacturing process. This was first relieved by heating the films to 90℃, upon which they shrank roughly 10% along one direction. Trilayers were prepared by compression molding the SEPS rubber pellets between sheets of the LLDPE films. The thickness of the rubber was maintained using steel strips as spacers. A platen press (Carver) was used at a temperature of 133℃. The trilayers were then cut into dogbone shapes for tensile testing.

Tensile testing was conducted in a MTS Insight tensile testing machine with a 50N load cell. The nominal test length of the sample (i.e. the distance between the clamps) was ~40 mm, whereas the gauge length of the samples was 20 mm. In the first step, dubbed "stretching", the samples were stretched to the desired strain (50% to 300% based on the

nominal test length). Immediately after reaching the desired strain, the samples were allowed to contract, a step dubbed “recovery”. The test was stopped when the force recorded reduced to low values and/or the samples bowed visibly.

The testing speed in most of the samples was 100% per minute based on the nominal test length. Limited experiments were conducted at lower (50%/min) and higher (200%/min) speed to verify that test speed did not affect results significantly.

The entire tensile tests were video-recorded and actual strains were obtained from displacement of markers placed on the sample surfaces.

Determining the wrinkle profile requires an edge-on view of the wrinkles. However, the fact that the face layers are capable of large plastic deformation complicates this situation. First, cutting dogbones may already induce some damage near the edges (even before any stretching), thus, in order to avoid biasing results from edge effects, it is desirable to image the wrinkles near the centerline. Yet, one cannot simply slice along the centerline of the wrinkled samples with a razor: once again, plastic deformation of the face layers induces massive distortion of the wrinkle structure. It is also difficult to cryo-fracture the samples since a length-wise fracture would be needed to see the wrinkle profiles. Accordingly, the samples were embedded in a liquid silicone rubber precursor (Sylgard 184) which was allowed to cure, thus replicating the sample topography in silicone. Since the silicone does not adhere strongly to LLDPE, the samples could readily be pulled away from the rubber, the silicone cut, and imaged by optical or scanning electron microscopy.

Finally, the strain mismatch induced in these samples is severe and hence delamination is a potential concern. A notable omission from the patent by Krueger et al. [95] is any discussion of delamination, and hence it is not clear whether the face sheets remain bonded to the elastomer in all cases. In research on SEPS-PP-SEPS composites, Hu et al.[96] did test for delamination by conducting repeated stretching-recovery tests and concluded that

delamination did not happen in most cases. We tested for delamination more directly by examining the samples in SEM as well as in optical microscopy. In occasional cases, some delamination near the edges was evident, but it stopped within 2-3 wavelengths of the edge. The contrast between delaminated and adhered films is very clearly obvious (Fig. Appendix C.1). Attempts to peel the face layers off from the rubber were unsuccessful. Thus we conclude that in our materials, delamination does not happen.

4.3 Result and Discussion

4.3.1 Mechanical Behavior

Fig. 4.2 illustrates the tensile behavior of the rubber, the plastic, and the trilayer, along with the images extracted from videos of the process. Here the nominal strain, $\epsilon_{\text{nominal}}$, on the x-axis is simply the change in length of the dogbone sample (displacement of the crosshead of the testing platform) relative to the original sample length. The tensile data for SEPS (Fig. 4.2D), shows behavior typical of elastomers: a low modulus (3.3 Mpa) during stretching, and only modest hysteresis during recovery, with an unrecovered strain of a few percent. The corresponding video frames (Fig. 4.2D) show that the strain is homogeneous.

The LLDPE shows behavior typical of a semicrystalline polymer: a modulus of ~400 MPa, followed by yielding at a few percent strain. Note that the stress of the LLDPE has been scaled by a factor of 0.1 in Fig. 4.2D. The corresponding images from videos (Fig. 4.2A) show that the yielding is accompanied by strong necking, and as deformation increases, the neck grows by drawing in surrounding material. Despite the stability of the neck, the plastic layer typically fails at less than 70% nominal strain. Accordingly, in Fig. 3, the sample was only stretched to 50% nominal strain before reversing the stretching. During recovery, strong

hysteresis is evident, with the force dropping rapidly to zero with very little recovery. Indeed the video shows that this small recovery corresponds to the portion of the sample that was not necked; the necked region itself shows negligible recovery (too small to be measured by our video imaging).

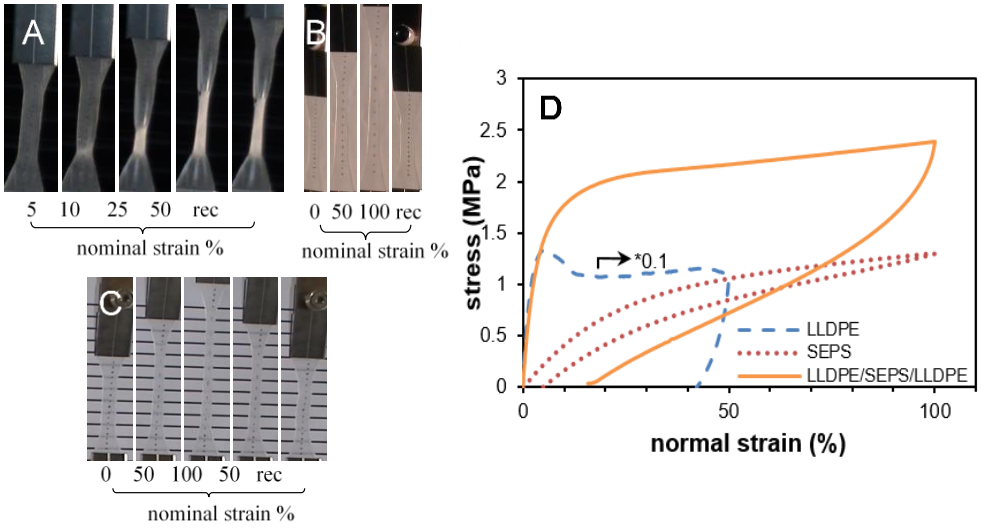

Figure 4.2. Images extracted from videos of the stretching dogbone specimens of (A) LLDPE, (B) SEPS, (C) trilayer with 860 micron SEPS midlayer. Nominal strains are noted below each image. "rec" denotes the final recovered state when the stress is nearly zero. (D) Engineering stress vs nominal strain for all three samples. The data for the LLDPE have been multiplied by a factor of 0.1

The behavior of the trilayer combines characteristics of both the rubber and the plastic: on one hand there is large hysteresis in stretching vs recovery. On the other hand, the deformation is homogeneous with no apparent necking, and the sample recovers its original length almost completely.

Fig. 4.3 shows the stress-strain curves as the nominal strain is varied from 50% to 300%. The early portion of the stretching curves is an indicator of the typical sample-to-sample variability. All the qualitative features noted above apply at all these strains: (1) at all these strains, samples did not show any apparent non-homogeneity or necking during stretching; (2) at all strains, there is significant hysteresis in the stretching vs release curves,

(3) yet all recover a considerable portion of the applied deformation. Quantitatively however, it is apparent that the irreversible deformation increases with the applied deformation. Incidentally, similar experiments were conducted for the SEPS itself, and the corresponding results, in the form of load vs elongation, will be presented in Fig. Appendix C.3 later.

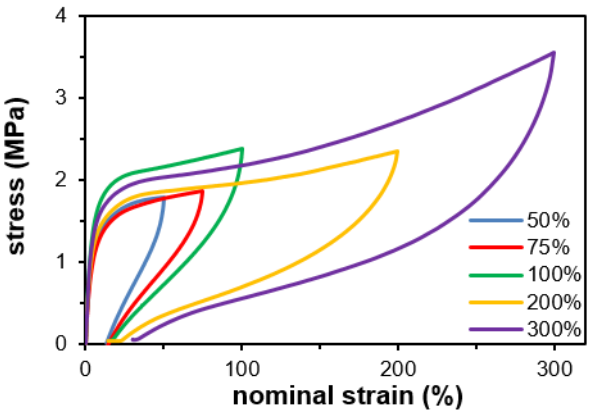

Figure 4.3. Engineering stress vs nominal strain for the trilayer samples with 860 micron SEPS midlayer.

From a fundamental perspective, the actual local strain is more relevant than the nominal strain, and hence it is more useful to express all results in terms of the local stretch, S. All the relevant geometric quantities are defined in Fig. 4.4A which illustrates the samples at four important points along the deformation path: the initial condition, the point of maximum stretching when the stretch is S_s, the critical point at which wrinkles first appear at a stretch of S_c (discussed below), and the final recovery when the stress drops to zero at the stretch S_r. Fig. 4.4B&C compare the local stretch values, from video analysis for the rubber and the plastic at the end of the stretching step (S_s), and at the end of the recovery step (S_r). A few points are noteworthy. First, the local stretch S_s in Fig. 4.4B is larger than $(1 + \epsilon_{\text{nominal}})$, presumably because the wider end-sections of the dogbone stretch much less than the gauge section. Second, from Fig. 4.4C, the rubber recovers almost completely, with a less

than 10% change in length even after being stretch to five times its original length. Third, from Fig. 4.4C, the irreversible deformation S_r of the trilayers increases with S_s, as already remarked above.

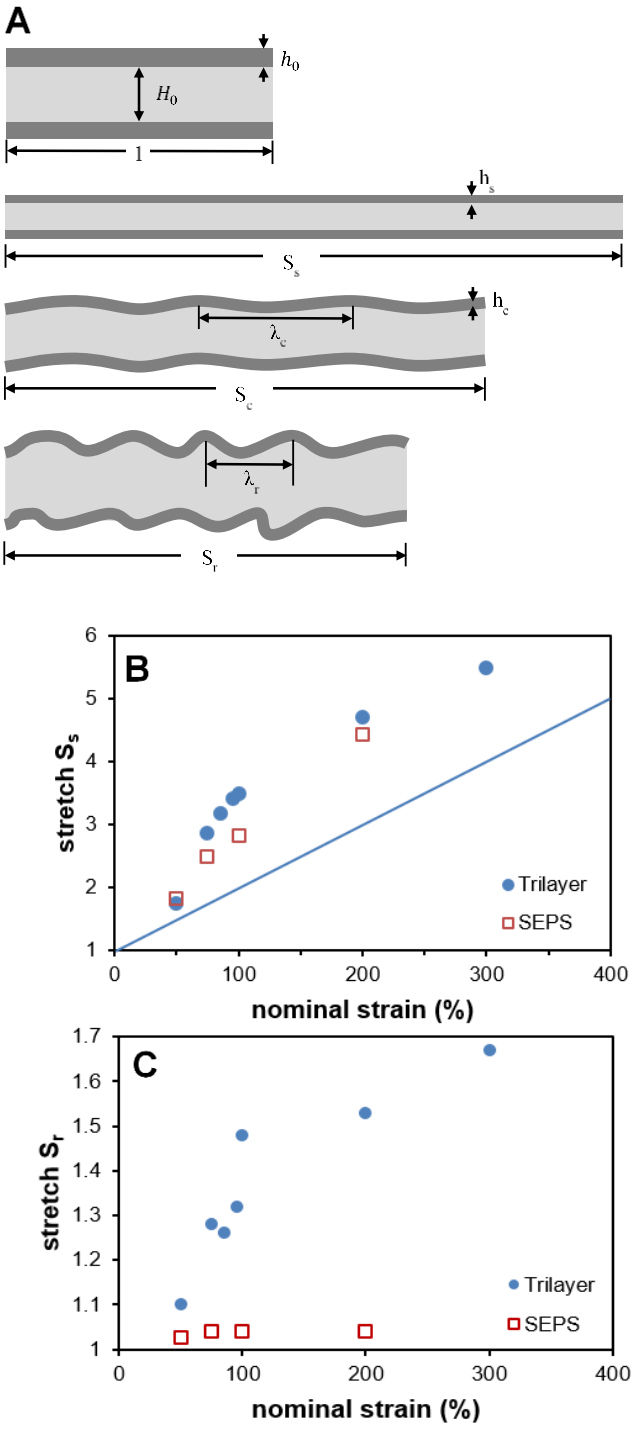

Figure 4.4. (A) Definitions of terms. (B) Stretch values at the end of the stretching step, and (C) at the end of the release step.

Limited video analysis of the stretching of free-standing LLDPE films was also conducted and shows that the stretch of the necked region reaches 4 at very small nominal strain, with only a slight increase with a further increase in nominal strain. The recovery of the necked region is negligible (i.e., cannot be estimated reliably by video analysis).

We now turn to the surface wrinkling phenomenon which motivated this research. At the lowest nominal strain tested, 50%, at the end of the recovery, the dogbone samples appear smooth with no visible wrinkles. Above 70% nominal strain, wrinkles are readily visible, but they are not uniform and certain regions of the dogbone samples may appear smooth. For strains exceeding 100%, the entire samples appear uniformly wrinkled. Fig. 4.5A shows optical images of the wrinkle profiles. It must be emphasized that these profiles are not cross sections of the samples themselves, but instead silicone replicas of the sample surface far from the edge. As such, they are negatives, i.e. the "peaks" of the original samples appear as "troughs" in the replicas.

From such images, the buckle wavelengths λ_r and amplitudes A corresponding to the recovered samples can be estimated. These are plotted in Fig. 4.5B. Amplitude/wavelength ratios exceeding 0.4 can be realized; with the exception of solvent swelling, such large amplitude buckles are difficult to realize by other methods. It is also noteworthy that films supported in soft solid substrates tend to undergo higher order instabilities such as folding or period doubling at large compression[1, 9]. Such complex post-buckling behavior is not evident in these plastic-rubber composites; instead buckles remain roughly monomodal, even though their profiles are not quite sinusoidal. It is apparent, even from cursory examination of the raw images (Fig. 4.5A), that the buckle wavelength reduces with increasing strain. Quantitatively this decrease in wavelength exceeds two-fold (Fig. 4.5B).

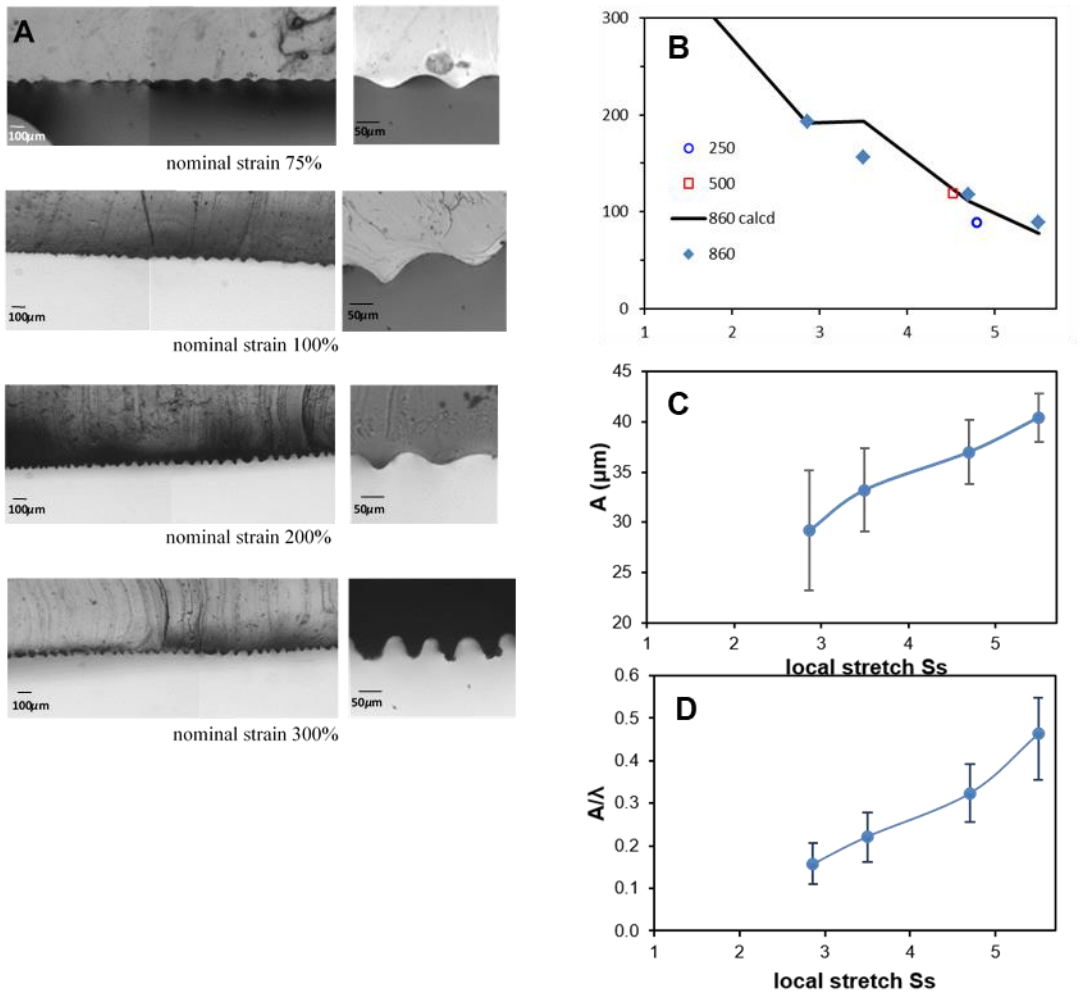

Figure 4.5. Images taken by inverted microscope: from top to bottom are 100% elongation (4X), 200% elongation (4X) and 300% elongation (20X) respectively; Fig. B-D: the wavelength, amplitude, and their ratio (A/λ) vs. local stretch.

Finally, a limited number of experiments were conducted on trilayers with lower rubber thicknesses, and the corresponding load-strain curves are shown in Fig. Appendix C.2. The overall load reduces with decreasing rubber thickness, but otherwise the shapes of the curves remain qualitatively similar. Despite this apparent similarity as rubber thickness reduces, there is actually a significant change in deformation behavior: the trilayers with 500 or 860 micron rubber thickness deformed homogeneously; the trilayer with 250 micron rubber thickness showed significantly non-homogeneous deformation, whereas the trilayer with 100 micron rubber thickness showed unambiguous necking (see Fig. Appendix C.2) along the width direction albeit not as severe as the free-standing plastic layers.

4.3.2 Elastic Model and Its Limitations

The previous research in this area has interpreted all the results in terms of elastic effects[95, 96]. The essential idea is to think of the film plasticity as having one – and only one – consequence, viz. creating a geometric mismatch when the layered composite is stretched. In this picture, during the stretching phase, the plastic layers undergo irreversible deformation, but the subsequent buckling mechanics are entirely interpreted by assuming linearly elastic behavior of both layers. This “elastic-during-release” approach is illustrated in section Appendix C.4 and it conceptually follows Hu et al.[96], except that the stretching-induced thinning of the film is accounted for, and all the analysis is conducted in terms of actual rather than nominal strain. The physical picture underlying Appendix C.4 is as follows: elastic films supported on softer elastic substrates are known to wrinkle when some critical compressive stress is reached[3]. When this critical stress is reached (at a stretch S_c) during release, wrinkles of wavelength λ_c appear everywhere on the film. The wavelength then

reduces further as release continues. With the assumptions listed explicitly in Appendix C.4, we culminate in the Eq. (AC. 4), which predicts the wavelength in terms of various geometric parameters and material properties. This equation can reproduce the changes in wavelength with stretching (Fig. Appendix C 7), albeit with one fitting parameter (see Appendix C.4).

With a more detailed analysis, further predictions may be made. For instance, if the film is much stiffer but much thinner than the rubber layer, one may assume that the contour length of the film is preserved after it buckles, an assumption dubbed "inextensible film" in the wrinkling literature[9]. This would then provide a geometric relationship between amplitude, wavelength, and S_c/S_r. In principle, it is also possible to construct an exact mechanical model which can calculate S_r from minimizing the total energy which is a sum of the stretching energy in the rubber layer and the bending energy of the film.

However these approaches depend on the assumption that the *only* role of film plasticity is to create a geometric mismatch, and therefore create an internal stress which compresses the face layer. In fact, plasticity can affect the process in many other ways. The first is the possibility of necking during stretching. As explained above, a free-standing LLDPE layer, and a trilayer with a 100 micron thick rubber midlayer both undergo obvious necking along the width direction. In contrast, the thickest trilayers (860 micron rubber midlayer) do not. However even for the latter sample, necking along the thickness direction – which would cause the LLDPE layer to become non-uniform in thickness in the fully-stretched state – cannot be ruled out. Indeed Li and Suo[97] have shown that upon stretching a plastic layer bonded to an elastomeric layer, for certain values of the geometric and material parameters, the plastic layer undergoes multiple necking, i.e. the plastic layer thins at numerous equally-spaced locations along the samples. For other parameter values, there was catastrophic necking at one location (i.e. the plastic layer failed) or there was uniform thinning of the plastic layer. That research was conducted for the specific case of metal films

(which deform plastically) bonded to elastomers, but the same physics are relevant here: the rubber layer "isolates" one region of the film from the other, and hence a single neck does not necessarily dominate the entire sample. If multiple necking does happen during deformation, then during the recovery phase, it is plausible that the thinner regions will buckle first. We have conducted limited experiments to test for this possibility (see Appendix C.3). These experiments suggest that thickness-direction necking does not happen in our samples: instead, the plastic layer undergoes uniform thinning. Nevertheless, depending on the mechanical properties of the rubber and the plastic, non-uniform thinning of the plastic layer may be a possibility. This would violate one of the key assumptions underlying Appendix C.4.

Secondly, plasticity may have a large effect during the release step. The face layers experience compressive stress during release; if this stress exceeds the yield strength, the face layer may yield in compression even before buckling. Yin and Chen[18] have examined this situation numerically for biaxial compression and concluded that if the plastic layer yields prior to buckling, the subsequent wrinkle pattern is strongly affected. Indeed our own experiments strongly indicate in-plane yielding: films stretched to 50% nominal strain recover almost completely but do not show wrinkles even though this strain greatly exceeds the yield strain of the plastic. To test for this more directly, we stretched a trilayer film with 860 micron thick rubber to a nominal strain of 200%, but the release was interrupted at a nominal strain of 150% at which no wrinkles appeared. This was followed immediately by re-stretching to 200%. The corresponding load-strain curve (Fig. 4.6A) shows significant hysteresis upon re-stretching, which may be quantified crudely by subtracting the rubber load from the plastic load (dashed green line in Fig. 4.6A). In contrast, the free-standing rubber layer shows no significant hysteresis in this same experiment. Thus the likely cause of hysteresis is that the plastic film accommodates at least a portion of the compressive strain by

in-plane yielding rather than wrinkling. Other potential mechanisms, e.g. some dissipative processes of interfacial failure, cannot be ruled out.

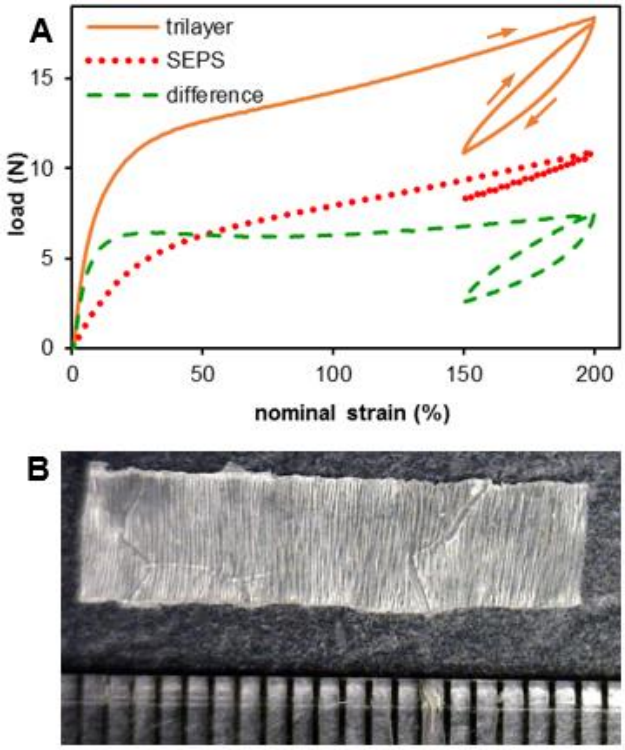

Figure 4.6. A. Partial release followed by restretching for a trilayer and SEPS rubber. Dashed green line is a point-wise subtraction of the SEPS and the trilayer. B. Image of one of the LLDPE plastic face layers recovered after dis-solving the SEPS elastomer in toluene. Each marking on the ruler corresponds to 1 mm.

Third, the elastic model in Appendix C.4 presumed plane-strain conditions, whereas the experimental samples have only a modest width with no constraints along the edge direction. Accordingly, during the release step, the trilayer sample increases in width. If the rubber is sufficiently thick, the kinematics of this deformation correspond to unidirectional compression, and therefore the width would increase by a factor of $\left(\frac{S_s}{S_r}\right)^{0.5}$ during the entire release step. The corresponding strains far exceed the ~2% yield strain of the plastic layer, i.e. the face layers may stretch irreversibly in the perpendicular direction during recovery.

Finally, after wrinkling, there may be localized plastic deformation at the points of highest curvature. Since the deformation is tensile on one surface of the plastic layer, and compressive on the opposite face of the same layer, the plastic layer is expected to yield in bending and form plastic hinges. The simulations of Takei et al.[98] indicate that such plastic deformation leads to an increase in curvature and a narrowing of ridges. To test for this possibility, samples stretched to 200% nominal strain were immersed in toluene, a solvent which dissolves the rubber mid-layer, but leaves the face layers undamaged. Fig. 4.6B shows a photo of the plastic face layers recovered from this experiment and it is clear that they maintain their ruffled appearance and do not relax back to a flat state. Similar ruffles are evident in Fig. Appendix C 1. when the LLDPE face layers are no longer bonded to the elastomer; in that case solvent was not needed since the films spontaneously delaminated at the sample edges. Both these images establish beyond doubt that the films do not behave elastically during release, and that plastic hinges are formed. To what extent they influence the mechanics is difficult to establish experimentally. Incidentally we note that for very small film thicknesses, such plastic deformation may appear at much smaller strains than expected from their bulk behavior[99].

In summary, while treating the layers as elastic provides a qualitative explanation of why wrinkling appear, plastic deformation is expected to have significant consequence even during the release step. Clear insight into the factors driving the buckling require a much more detailed consideration of how plastic deformation. For this we turn to numerical simulations.

4.4 Simulations

Simulations were conducted by a collaborator, Sameer Damle, in consultation with the author, Junyu Yang.

A custom-developed nonlinear 3D finite element analysis program was used to conduct all the FE analyses in this chapter. The overall goal of the simulations is not to capture the quantitative details of the deformation and wrinkling process, but to explore qualitatively the mechanical phenomena that are important to produce surface instabilities during stretching and subsequent release of the thin film. Accordingly, we used the simplest constitutive behavior that can capture the pure component behaviors of the rubber and the plastic layers. The rubber was modeled as a 2-parameter Mooney-Rivlin material. The LLDPE face layer was modeled as a neoHookean material up to the yield point, and behaved as a perfectly plastic material after yielding, i.e., maintained a stress equal to the yield strength without any strain hardening.

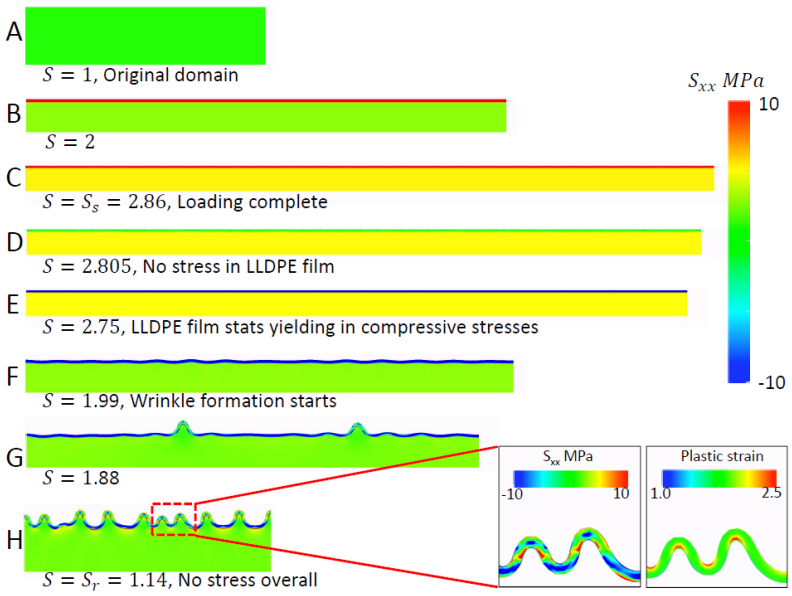

Figure 4.7. Snapshots of the domain during loading and unloading simulation. Yield strength of plastic film is 10 MPa. Contours of Sxx stress are shown.

Fig. 4.7 shows snapshots at various points during the stretching (to $S_s = 2.86$) and subsequent release of the trilayer film. This value of 2.86 roughly corresponds to the actual stretch in the 75% elongation experiment. The distributions of the Cauchy stress S_{xx} are shown as colormaps. During the stretching step, both layers thin uniformly (this will be discussed further later). As expected from the constitutive equation, the plastic layer yields at a stretch of roughly 1.025 (not shown), and thereon for the remainder of the stretching step, the stress in the plastic layer remains constant at σ_y.

Upon release, the initial recovery behavior is as expected: the stress in the plastic layer reduces elastically, reaches zero at S=2.805 (Fig. 27D), and subsequently becomes compressive. However, when the compressive stress reaches σ_y at a stretch of 2.73 (Fig. 27E), the plastic layer starts yielding in compression. Upon further release, at a stretch of about 1.99, wrinkles appear. It is remarkable that there is a large range of stretch (from 2.73 to 1.99) within which the film accommodates the compression by yielding in-plane without developing wrinkles. Once wrinkles appear, they grow as the film recovery continues and the simulation is stopped at $S_r = 1.13$ when the net load in the computational domain reaches zero. The non-uniformity of the wrinkle growth is striking: some buckles grow to a large amplitude much earlier than others. The random thickness variation in our computational model may have introduced the hetergeneity responsible for growth of localized folds as suggested by Semler et al.[100], albeit for purely elastic systems. This apparent non-homogeneous growth of wrinkles resembles the “ridge” mode explored previously[6, 101, 102] where tall localized ridges appear in elastic/elastic bilayers when the substrate is prestretched. However in that case, the wrinkles surrounding each ridge tend to reduce in amplitude when a ridge is formed, a feature that is not evident in Fig. 9. Despite the simple model of plasticity and the plane strain assumption, the average spacing between the

simulated wrinkles (~230 micron) is close to that observed experimentally (~180 micron) at a similar stretch.

The inset to Fig. 4.7 examines in greater detail the Cauchy stress S_{xx} and the local plastic strain in the film at the end, i.e. at $S_r = 1.13$. It is immediately apparent that film bending induces differential yielding along the thickness direction. While the film as a whole is under compressive load, the outer surface of the film at the crest of the wrinkles experiences tensile stress and thus yields in tension. On the other hand, the inner surface of the film at the film-rubber interface is under compressive stresses. The stress state is opposite at the troughs with tensile and compressive stresses at the inner and outer surfaces, respectively. Thus, there are large plastic strain gradients through the thickness of the film at the peaks and troughs of the wrinkles giving rise to "plastic hinges" at these locations. These hinges cause the shape of the wrinkles to deviate from the sinusoidal profile common in elastic material systems, and permit the development of high aspect ratio wrinkles.

It is noteworthy that the simulations contradict all of the assumptions of the elastic model[96] of Appendix C.4: (1) Eq. (AC.1) assumed that wrinkles appear when both materials are elastic, whereas the simulations suggest that the face layer yields prior to buckling; (2) Eq. (AC.2) assumed that the film thickness remains at h_s during release whereas simulations suggest that the film thickens as it yields prior to buckling; (3) wrinkles were assumed to grow uniformly everywhere, whereas the simulations show that some buckles grow much earlier than others; (4) Eq. (AC.3) assumed that the existing buckles simply reduced in wavelength (and increased in amplitude) while remaining roughly sinusoidal, whereas in the simulation, wrinkles profiles show highly localized curvature; (5) finally, the physical picture of Appendix C.4 assumed that the film experienced compressive strains everywhere, whereas the formation of plastic hinges in the inset to Fig. 4.7 indicates that at some locations, the film undergoes large tensile deformation.

The take-home message of the simulation work is as follows: for stretch-and-release induced wrinkles, as the yield stress of the face layers increases, stretching – and therefore subsequent wrinkling – become increasingly non-homogeneous. Combined with the conclusions of Section 4.3.1, we therefore conclude that stretch-and-release will generate uniform wrinkles only in a finite window of material properties. Stretch-and-release will produce non-homogeneous wrinkles if the yield strength is too high, and no wrinkles if the yield strength is too low.

4.5 Conclusion

In summary, we have examined the surface wrinkling of composite films composed of an elastomeric layer sandwiched between two plastic face layers, an idea originally patented by Krueger et al. [95] The stretching of the initially smooth composite films leads to a geometric mismatch: since the plastic layers yield during stretching, the stress-free length of the plastic layers is longer than that of the elastomeric midlayer. Upon releasing, the film develops an internal stress, and the face layers undergo compression-induced buckling, resulting in a heavily wrinkled surface. High aspect ratio wrinkles – with the amplitude to wavelength ratio exceeding 0.4 – can be realized.

This project points to numerous features of the stretch-and release process that were not recognized previously. [95, 96, 103] Specifically, plasticity of the face layers plays a key role at all stages of this process. The most obvious role, tensile yielding and irreversible increase in length during stretching, has already been recognized previously. In addition, simulations show (1) compressive yielding during release, (2) the formation of plastic hinges

as wrinkles develop, and (3) non-uniform thinning during stretching (i.e. necking in the thickness direction) if the yield stress of the films is high or rubber thickness is small. These last results were not shown in the chapter because they resulted from the work of Sameer Damle, but are described in the published paper.[104] Of these simulation predictions, our experiments unequivocally confirm plastic hinge formation, and strongly support in-plane yielding. We do not see thickness direction necking, at least at the single thickness examined in detail. However, width direction necking is clearly evident at small rubber thicknesses.

Taken together, the simulations suggest that stretch-and release can produce uniform wrinkles only within a finite range of material properties. If the yield stress is too low, wrinkles are not expected since the face layers accommodate compression by in-plane yielding. If the yield stress is too high or the rubber thickness is too low, necks are expected and wrinkling is expected to become increasingly non-homogeneous over the surface. This is of obvious relevance to designing films that seek to exploit stretch-and-release to create wrinkled surfaces.

5.0 Summarization and Conclusion of This Dissertation

Two of the three projects listed in the Introduction are completed. They are: (2) Stretching-induced wrinkling in plastic-rubber composites. This resulted in one published paper in Soft Matter with the same title. (3) The preparation and thermomechanical properties of high temperature PPEK foams. One paper is on PPEK foam development is close to submission. Another paper reviewing the current state of high temperature foams is also in progress.

For project (1): compression-induced fold localization of thin films bonded to viscous substrate, the effect of strain rate, sample width and liquid layer thickness to the buckling and folding of the thin film has been systematical studied. Also, future work is being conducted with the following direction: 1) Try to pin-down the certain minimum strain needed for showing folding localization. 2) Better understanding the role of the long edge of the film in the wrinkling folding process. 3) Better understanding the sensitiveness to small flaws of the wrinkling process or the fold localization.

For project (2): stretching-induced wrinkling in plastic-rubber composites, the mechanics of three-layer composite films has been examined. The mechanism for this strecth-induced wrinkled texture is that during stretching, the plastic layers yield and stretch irreversibly whereas the elastomer stretches reversibly. Thus, upon releasing, the plastic layers buckle due to compressive stress imposed by the elastomer. High aspect ratio wrinkles – with the amplitude to wavelength ratio exceeding 0.4 – can be realized. Also, with help of simulation, the effect of plasticity of the face layers has been studied in this project. However, for further improving the results, the constitutive models used in this research could be adjusted and modified somehow to try to better tackled the full parameter space of the

experiments. This may do the favor of better studying the effect of rubber layer thickness to the wrinkling of this system.

As to project (3): the preparation and thermomechanical properties of high temperature PPEK foams, a method of producing PPEK foam has been developed, the cell morphology has been studied and foam properties, mainly thermal conductivity and modulus have been studied as a function of foam density. The potential advantage of poly(phthalazinone ether ketone) (PPEK) is that, being an amorphous polymer, the foaming can be controlled precisely via the foaming temperature. Future work should consider following directions: 1) Being thermoplastic, it is possible to shape the PPEK foam, e.g. by molding. This provided an excellent potential application field, i.e. beads foaming. Bead foam is an effective way to package many consumer products. The physical properties of the beads provide many advantages. Unique in its insulation qualities, this material has the ability to be safe from impact or heat. In addition, beads also offer flexibility and strength. Another application is filler in concrete mixtures. With the right allotment, the end result is a substance that is solid and secure but also lightweight. [105, 106] Foam can be reshaped with PPEK foam beads, which may favor the customers' needs, i.e., that the end user can shape the foam as desired. Some preliminary study has been conducted to test out the feasibility. Up to now, we found that separated foam disks can be re-molded together at about 250℃ (See Fig.5.1 below). Smaller foam particles have also been tested out, but they were unsuccessful. The reasons for this might be following: (a) By comparing with the foam disks, the contact area of the beads might be lower, which may affect them to stick to each other. (b) The PPEK foams prepared have a thin layer shell overwrapping the foam. The shell might also prevent them stick to each other. 2) Since PPEK can be foamed successfully, other members of the same family (poly(phthalazinone ether sulfone) or poly(phthalazinone ether sulfone ketone) which have even higher glass transition temperatures) may also be foamed by the same

methods. The same methods could also be expanded to foam copolymers of phthalazinone-based polymers. For the purpose of preparing HTFs with more kinds, this might be the future research certainly worth digging into.

Figure 5.1. Two foam disks re-molded together at about 250°C.

Appendix A The Preparation and Thermomechanical Properties of High Temperature Foams

PPEK: Poly (phthalazinone ether ketone)

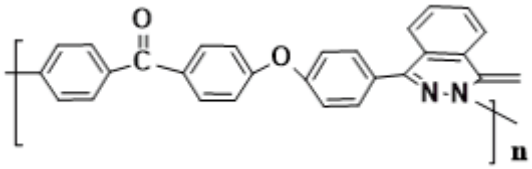

PPES: Poly (phthalazinone ether sulfone)

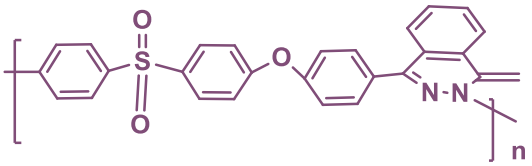

PPESK： Poly (phthalazinone ether sulfone ketone)

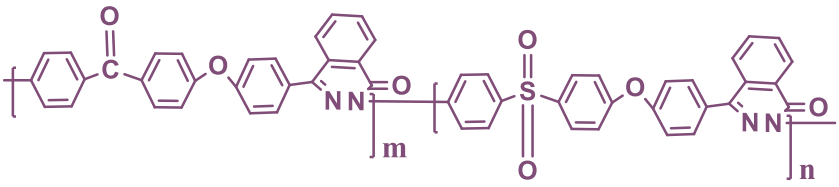

Figure Appendix A. 1. Structures of phtalazione based polymers

Appendix A.1 GPC Measurement for Pure PPEK:

Number-average molecular weight of the PPEK (Mn) equals to 18816 g/mol; mass-average molecular weight of PPEK (Mw) equals ot 37724 g/mol.

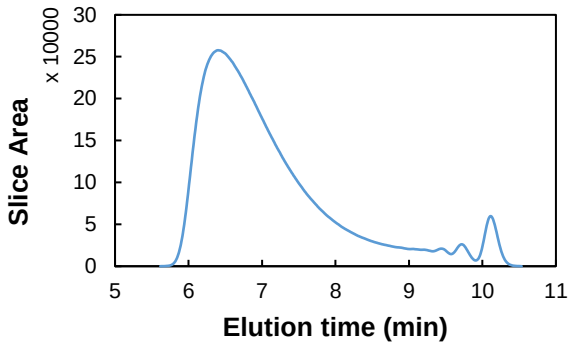

Figure Appendix A. 2. GPC measurement for pure PPEK

Appendix A.2 DSC Measurement for Pure PPEK:

T_g of pure PPEK sample measured from DSC is shown to be at 261.66°C.

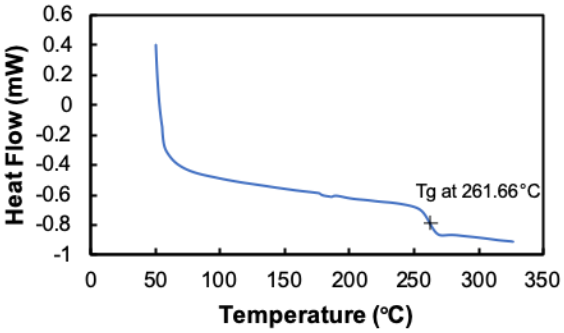

Figure Appendix A. 3. DSC measurement for pure PPEK

Appendix A.3 Table for Commercialized HTFs:

Table 1. Commercialized HTFs

Name	Material	Density (kg/m^3)	Maximum working temp. (^oC)
Specflex®	polyurethane	15	100
LAST-A-FOAM®	epoxy-urethane	290-640	117
Gurit® PVC HT	polyvinyl chloride(PVC)	60-80	140
ZOTEK® F	polyvinylidene fluoride	30-75	160
ZOTEK® N	polyamide (Nylon)	35-50	205
TegraCore™	polyphenylsulfone (PPSU)	53	204
INTEK®	polyimide	6.4	300
ROHACELL® A	polymethacrylimide (PMI)	32-75	130
Polydamp®	melamine Foam (PMF)	9	180
SOLIMIDE®HT-340	polyimide	6.4	300
BISCO® Silicones	silicone	350	200

Appendix B Compression-induced Fold Localization of Thin Films Bonded to Viscous Substrate

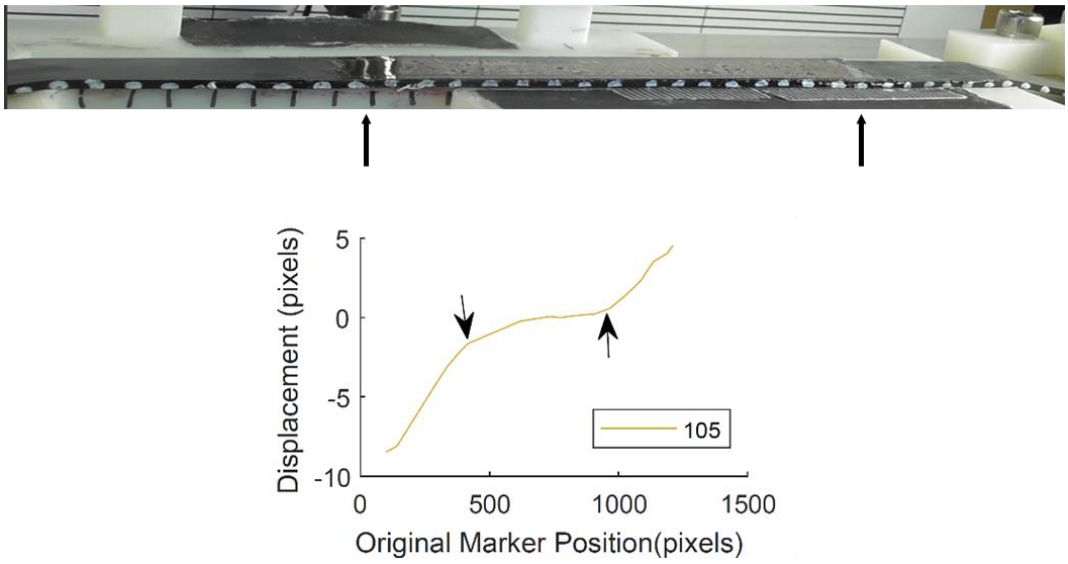

Figure Appendix B 1. The displacement profile of the markers across the entire rubber strip at one instant during the loading process. The arrows indicate the ends of the film. Note the higher strain in the rubber strip nearer to the clamps.

Appendix C Stretching-induced Wrinkling in Plastic-rubber Composites

Appendix C.1 Testing for Delamination

The geometric mismatch induced in these samples is severe and hence delamination is a potential concern. We tested for delamination directly by examining the samples in SEM as well as in optical microscopy. In occasional cases, some delamination near the edges was evident, but it stopped within 2-3 wavelengths of the edge. The contrast between delaminated and adhered films is very clearly obvious (Fig. Appendix C1). Attempts to peel the face layers off from the rubber were unsuccessful. Thus we conclude that delamination does not affect our experiments.

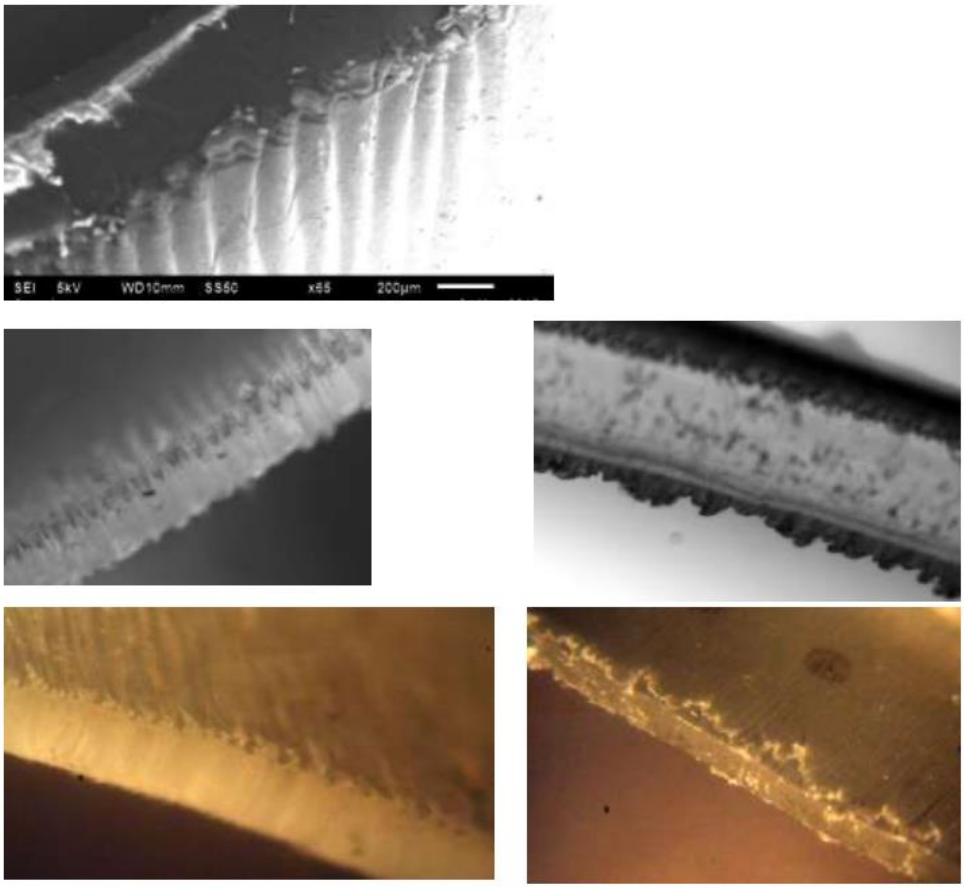

Figure Appendix C 1. Left column: SEM (top) and optical (lower) images taken within one day after stretching and releasing the trilayer composite samples showing complete attachment of the plastic film to the rubber. Right column: Optical images of delamination of the film starting from the edge of sample after four days. Note that the delaminated sections remain ruffled indicating plastic deformation in bending.

Appendix C.2 Experiments with Other Rubber Layer Thicknesses

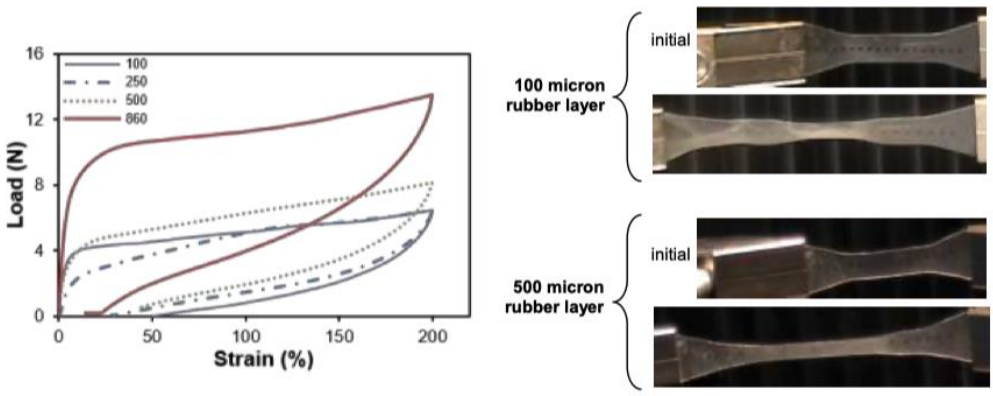

Figure Appendix C 2. Stress-strain curves of trilayer samples at various rubber layer thicknesses, H 0 , listed in the legend in microns. Curve at 860 microns correspond to the same data as in Fig. 4.3. The images to the right show the snapshots during stretching of two different trilayer samples. Note that the trilayer with 500 micron thick rubber (left) stretches homogeneously, whereas the one with 100 micron thick rubber (right) shows necking.

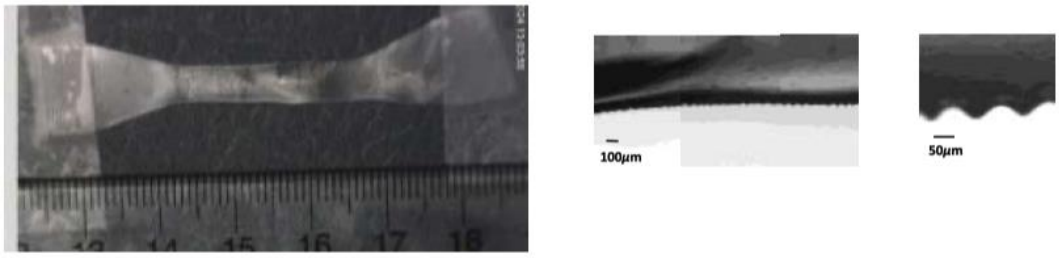

Figure Appendix C 3. Image of sample (left) with a 100 micron thick rubber layer with 50 micron face layers after 200% nominal strain. Right: optical images of cross sections of silicone replicas. Even at this small rubber thickness, wrinkles develop with nearly the same wavelength as Fig. 4.6 in the main text.

Appendix C.3 Experimental Tests for Necking of Trilayers

Two experiments were conducted to test for non-homogeneous thinning of the plastic layer in a trilayer. In the first, samples of the trilayers (with a rubber layer thickness of 860 micron) were stretched in a tension apparatus to a stretch of 2.4. Unlike the equipment used for tensile testing, this apparatus is not capable of measuring loads. However it permits examination of the samples at far higher resolution using a video microscope. This experiment was performed quasi-statically: the sample was slowly stretched to the final length, and allowed to stay stretched for several minutes during video examination. Non-homogeneous deformation was not evident in this experiment. Subsequently, the sample was gradually released with constant video microscopic examination. A key feature of the simulations (Fig. 4.7 in the main text) is that if necks appear, then during the subsequent release, the buckling is highly non-uniform: the thinned regions buckle first and develop a significant amplitude before the thicker regions buckle. Such localized buckles would almost certainly have been evident in video examination, but instead, we observed only a gradual increase in buckle amplitude everywhere over the sample.

A second experiment was conducted by stretching the samples to a stretch of roughly 2 in a different apparatus. A silicone rubber precursor liquid was poured over this sample while still stretched and allowed to crosslink. The silicone-embedded sample was then then placed in an oven at 70℃ while held stretched. At this temperature, the rubber layer relaxes its tension over several hours (i.e. a free-standing rubber layer recovers very little). Thus upon cooling, when the trilayer sample was extracted from the embedded silicone, it did not change dimensions significantly, i.e. the stretched state was preserved with very little wrinkling. The sample as well as the embedding rubber surfaces were then examined by optical microscopy. Note that this entire procedure is similar to that used for obtaining Fig.

4.1E, except that the silicone embedding was performed while the sample was held stretched. Both were found to be smooth with no evidence of non-homogeneous thinning. The corresponding silicone replica is shown in Fig. Appendix C 4. If the film had shown periodic necking behavior, it would likely have induced correspondingly periodic variations in the rubber thickness as well, but this is not evident in Fig. Appendix C 4.

The fact that these two altogether different experiments did not show evidence of necking suggests that the plastic film thins uniformly.

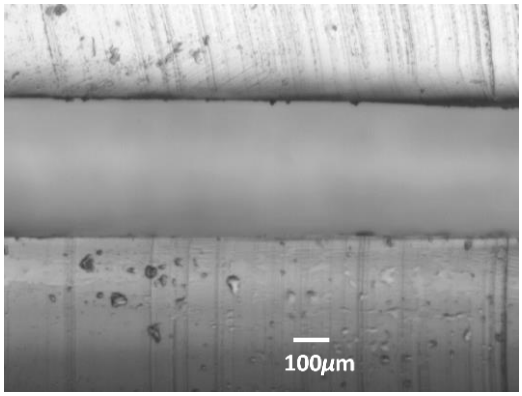

Figure Appendix C 4. Image of silicone replica of a sample stretched, embedded in silicone, and then heated. The silicone is an accurate replica of the stretched sample and shows no evidence of periodic variations in thickness.

Appendix C.4 Elastic Model

The physical picture is as follows: elastic films supported on softer elastic substrates wrinkle when some critical compressive stress is reached. When this critical stress is reached (at a stretch S_c) during release, wrinkles of wavelength λ_c appear everywhere on the film. Linear stability analysis of this situation under plane-strain conditions shows that[3]

$$\lambda_c = 2\pi h_{film}\left(\frac{\bar{E}_{film}}{\bar{E}_{substrate}}\right)^{\frac{1}{3}} \quad \text{(AC-1)}$$

where $\bar{E}_j = E_j/(1-\nu_j^2)$ is the modulus appropriate for plane strain conditions. In our experiments, h_{film} is 50 microns at the start of the experiment, but expected to change throughout the experiment. The value most relevant to the above equation is the film thickness h_c at the critical threshold for buckling. Since the free-standing plastic film does not undergo significant recovery, as a first approximation, the film dimensions are assumed to remain fixed during recovery. Thus, the film thickness during recovery can be taken to be

$$h_{film} = h_s = h_0 S_s^{-\frac{1}{2}} \quad \text{(AC-2)}$$

This equation assumes the kinematics of homogeneous uniaxial elongation. After buckling, as compression continues, the wavelength is expected to decrease geometrically in an accordion-like fashion to a final value:

$$\lambda_r = \lambda_c \frac{S_r}{S_c} \quad \text{(AC-3)}$$

Combining the above expressions yields

$$\lambda_r = 2\pi h_{film}\left(\frac{\bar{E}_{film}}{3\bar{E}_{substrate}}\right)^{\frac{1}{3}}\frac{S_r}{S_c} = 2\pi h_0 S_s^{-\frac{1}{2}}\left(\frac{\bar{E}_{film}}{3\bar{E}_{substrate}}\right)^{\frac{1}{3}}\frac{S_r}{S_c} \quad \text{(AC-4)}$$

We will now consider each of the quantities on the right hand side of Eq. (AC-4) in turn. S_r is directly measured experimentally (Fig. 4.4B). S_c is more difficult to quantify since we were unable to measure the critical stretch at the wrinkling threshold. Specifically, the buckle amplitude and wavelength are both relatively small, and not visible with the visualization methods used in our experiments. Limited experiments were conducted on a custom stretching apparatus in our lab using a higher magnification camera which could be mounted much closer to the sample. Even in that case, the critical stretch was difficult to judge accurately. How then can S_c be estimated? We will follow the approach of Hu et al.

[96] of using the stress-strain data to estimate S_c. This relies on the assumptions that the total force in the trilayer is a simple sum of the force in the rubber and the plastic, and that the load in the rubber layer in the trilayer is identical to the load in a free-standing rubber layer at the same nominal strain. Accordingly, we may estimate the load in the plastic layer at any nominal strain:

$$F_{plastic} = \frac{F_{trilayer} - F_{rubber}}{2} \qquad \text{(AC-5)}$$

The factor of 2 in Eq. (AC-5) simply accounts for the fact that there are two face layers. Figure Appendix C 5 shows the "raw data" of the $F_{trilayer}$ and F_{rubber} needed in Eq. (AC-5), and the $F_{plastic}$ so-obtained is plotted in Fig. Appendix C 6. It is interesting to note that the plastic contribution to the trilayer during the stretching is quite similar to the force of a free-standing plastic layer at the same nominal strain, i.e. coupling the plastic to the rubber (and hence suppressing necking) does not qualitatively change the stress-strain behavior of the plastic layer.

Regardless, during the release step, the calculated load in the plastic layer stays positive up to some value of nominal strain, beyond which it becomes negative. The point at which the load becomes zero may be regarded as the instant when the plastic first experiences compressive strain [96]. If we assume that the critical strain for wrinkling is quite small, then wrinkles must appear immediately after that point, i.e. the stretch at the zero load point may be regarded as nearly equal to S_c. The portion of the recovery step between S_c and S_r can then be regarded as compression beyond critical wrinkling. Fig. Appendix C 7B&C plot S_c, S_r and their ratio S_r/S_c, which is relevant to Eq. (AC-4).

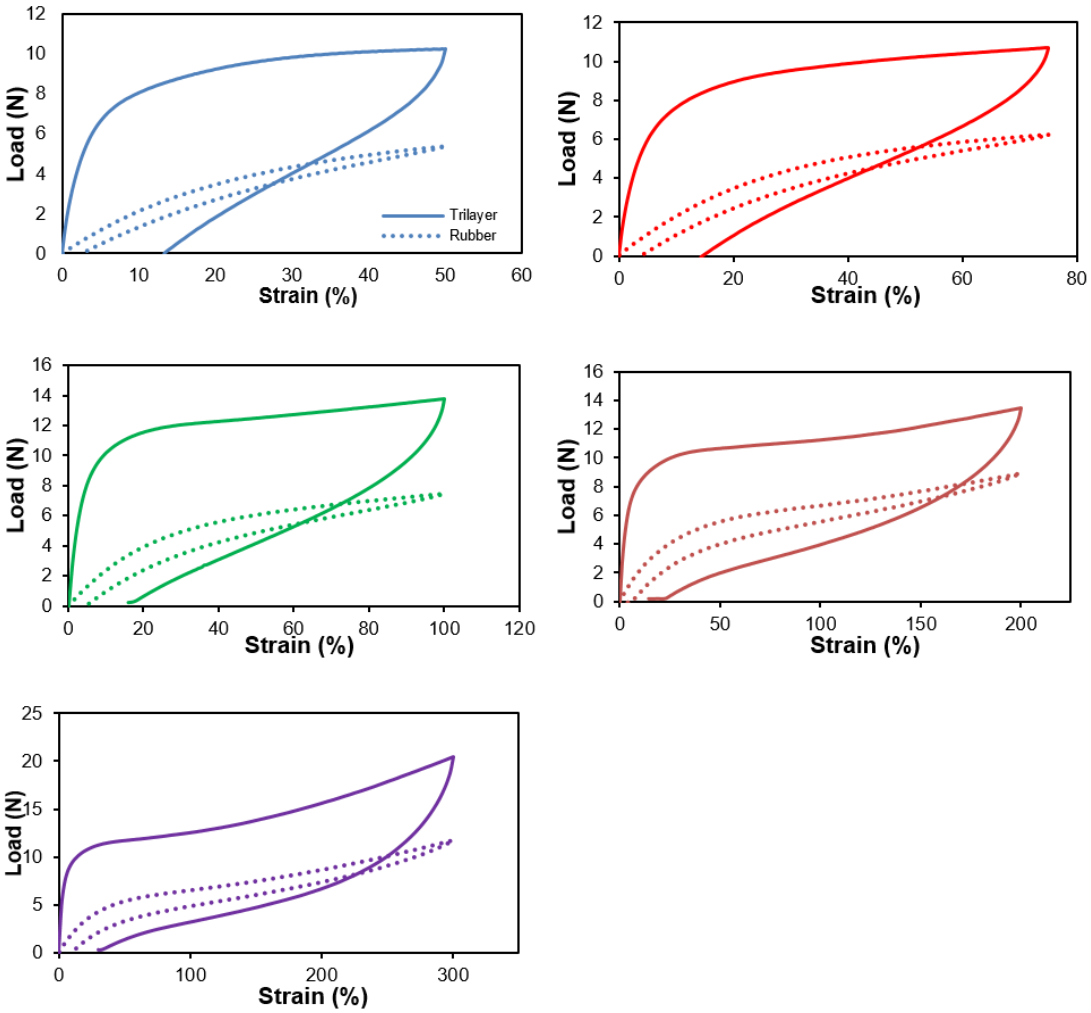

Figure Appendix C 5. Force vs nominal strain curves for the trilayer and the elastomer at various nominal strains. The difference between these curves corresponds to Fig. Appendix C 6A below.

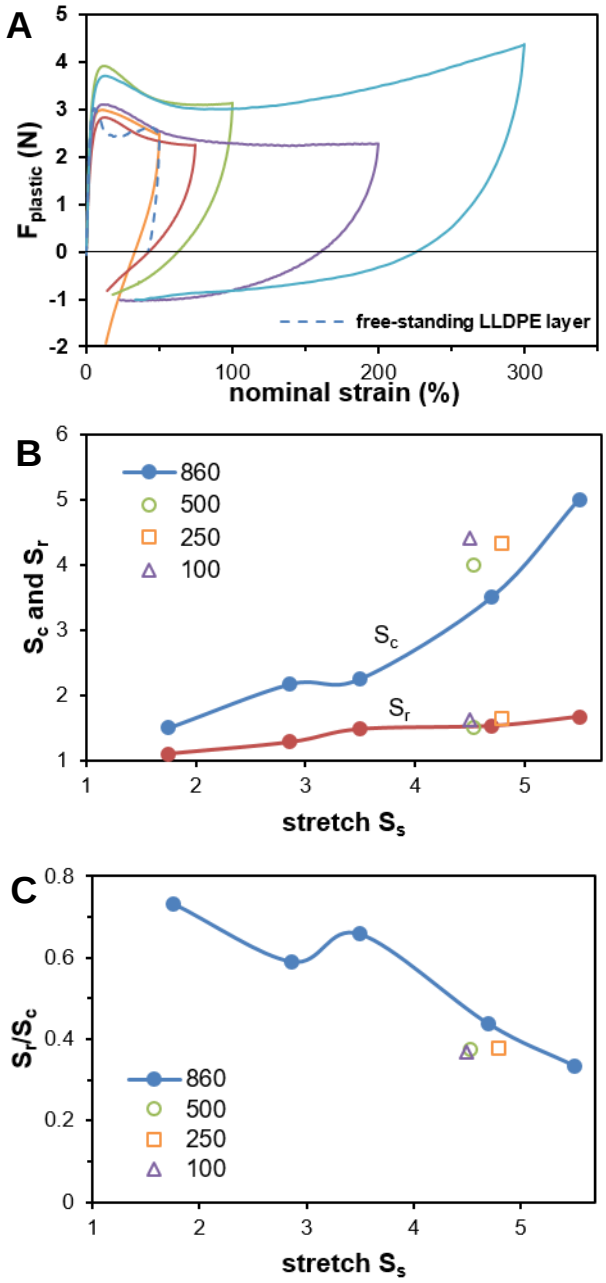

Figure Appendix C 6. (A) Load in the plastic layers calculated from Eq. (AC-5). See Fig. Appendix C 5 for the raw data used in subtraction. The dashed line corresponds to the same data as the LLDPE in Fig. 4.2D. (B) Stretch values *Sc* and *Sr*. The latter are the same data as in Fig. 4.4C. (C) Ratio S_r/S_c relevant to Eq. (AC-4).

The last remaining quantity in Eq. (AC-4) is the modulus ratio $\left(\frac{\bar{E}_{film}}{\bar{E}_{substrate}}\right)$. This is more difficult to estimate because what is relevant in Eq. (AC-4) is not the ratio of the zero-strain modulus, but the ratio of the effective modulus in the neighborhood of the critical strain. Since the critical strain itself changes with S_s, the corresponding modulus must change as well. For the plastic layer, the problem is further compounded by the fact that the strain-strain relationship of the yielded plastic layer is difficult to measure directly; it may not be the same as that measured during stretching and moreover, it may change with stretch. We have therefore used the modulus ratio as an adjustable parameter to compare Eq. (AC-4) against the data. The solid line in Fig. Appendix C 7 shows that reasonable agreement with the data is obtained if $\left(\frac{\bar{E}_{film}}{\bar{E}_{substrate}}\right)$ is taken to be 12 (any value between 10 and 16 gives comparable agreement). We must note however the modulus ratio of 12 used is much lower than the ratio (over 100) estimated from the small-strain region in Fig. 4.2D.

It is worth noting that Hu et al.[96] reported reasonable agreement between their model and experiments with no fitting parameters. However they ignored the fact that the plastic layer must become thinner due to stretching (i.e. they set $h_{film} = h_0$ instead of Eq. (AC-2), a very poor approximation given that their nominal strains were as large as 600%). If they had accounted for the thinning of the plastic layer, their model would have been in poor agreement with their experiments.

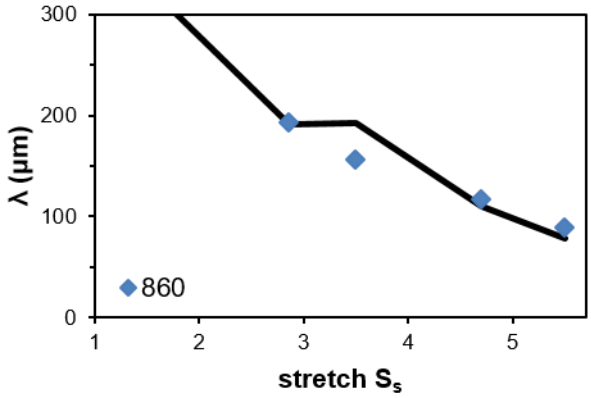

Figure Appendix C 7. Best fit of Eq. (AC-4) to the measured wavelength data. The data are the same as from Fig. 4.5a from the main text.

Bibliography

1. Brau, F., Vandeparre, H., Sabbah, A., Poulard, C., Boudaoud, A., and Damman, P., *Multiple-length-scale elastic instability mimics parametric resonance of nonlinear oscillators.* Nature Physics, 2011. **7**(1): p. 56-60.

2. Chen, X. and Hutchinson, J.W., *A family of herringbone patterns in thin films.* Scripta Materialia, 2004. **50**(6): p. 797-801.

3. Huang, Z.Y., Hong, W., and Suo, Z., *Nonlinear analyses of wrinkles in a film bonded to a compliant substrate.* Journal of the Mechanics and Physics of Solids, 2005. **53**(9): p. 2101-2118.

4. Jiang, H.Q., Khang, D.Y., Song, J.Z., Sun, Y.G., Huang, Y.G., and Rogers, J.A., *Finite deformation mechanics in buckled thin films on compliant supports.* Proceedings of the National Academy of Sciences of the United States of America, 2007. **104**(40): p. 15607-15612.

5. Bowden, N., Brittain, S., Evans, A.G., Hutchinson, J.W., and Whitesides, G.M., *Spontaneous formation of ordered structures in thin films of metals supported on an elastomeric polymer.* Nature, 1998. **393**(6681): p. 146-149.

6. Cao, Y. and Hutchinson, J.W., *Wrinkling Phenomena in Neo-Hookean Film/Substrate Bilayers.* Journal of Applied Mechanics-Transactions of the Asme, 2012. **79**(3).

7. Huang, J., Juszkiewicz, M., de Jeu, W.H., Cerda, E., Emrick, T., Menon, N., and Russell, T.P., *Capillary wrinkling of floating thin polymer films.* Science, 2007. **317**(5838): p. 650-653.

8. Holmes, D.P. and Crosby, A.J., *Draping Films: A Wrinkle to Fold Transition.* Physical Review Letters, 2010. **105**(3): p. 038303.

9. Pocivavsek, L., Dellsy, R., Kern, A., Johnson, S., Lin, B.H., Lee, K.Y.C., and Cerda, E., *Stress and fold localization in thin elastic membranes.* Science, 2008. **320**(5878): p. 912-916.

10. Chatterjee, S., McDonald, C., Niu, J., Velankar, S.S., Wang, P., and Huang, R., *Wrinkling and folding of thin films by viscous stress.* Soft Matter, 2015.

11. Sridhar, N., Srolovitz, D.J., and Suo, Z., *Kinetics of buckling of a compressed film on a viscous substrate.* Applied Physics Letters, 2001. **78**(17): p. 2482-2484.

12. Hobart, K.D., Kub, F.J., Fatemi, M., Twigg, M.E., Thompson, P.E., Kuan, T.S., and Inoki, C.K., *Compliant substrates: A comparative study of the relaxation mechanisms of strained films bonded to high and low viscosity oxides.* Journal of Electronic Materials, 2000. **29**(7): p. 897-900.

13. Huang, R. and Suo, Z., *Wrinkling of a compressed elastic film on a viscous layer.* Journal of Applied Physics, 2002. **91**(3): p. 1135-1142.

14. Im, S.H. and Huang, R., *Evolution of wrinkles in elastic-viscoelastic bilayer thin films.* Journal of Applied Mechanics-Transactions of the Asme, 2005. **72**(6): p. 955-961.

15. Chan, E.P., Page, K.A., Im, S.H., Patton, D.L., Huang, R., and Stafford, C.M., *Viscoelastic properties of confined polymer films measured via thermal wrinkling.* Soft Matter, 2009. **5**(23): p. 4638-4641.

16. Yoo, P.J. and Lee, H.H., *Evolution of a stress-driven pattern in thin bilayer films: Spinodal wrinkling.* Physical Review Letters, 2003. **91**(15).

17. Srinivasan, K., Subbarayan, G., and Siegmund, T., *Wrinkling on irreversibly deforming foundations.* Thin Solid Films, 2012. **520**(17): p. 5671-5682.

18. Yin, J. and Chen, X., *Buckling patterns of thin films on compliant substrates: the effect of plasticity.* Journal of Physics D-Applied Physics, 2011. **44**(4).

19. Cao, Y.-P., Zheng, X.-P., Jia, F., and Feng, X.-Q., *Wrinkling and creasing of a compressed elastoplastic film resting on a soft substrate.* Computational Materials Science, 2012. **57**: p. 111-117.

20. El Haitami, A., Bretagnol, F., Assuid, P., Petitet, G., Cantournet, S., and Corte, L., *Erasable and Reversible Wrinkling of Halogenated Rubber Surfaces.* Langmuir, 2013. **29**(50): p. 15664-15672.

21. Verdejo, R., Werner, P., Sandler, J., Altstadt, V., and Shaffer, M.S.P., *Morphology and properties of injection-moulded carbon-nanofibre poly(etheretherketone) foams.* Journal of Materials Science, 2009. **44**(6): p. 1427-1434.

22. Zhang, H.B., Yan, Q., Zheng, W.G., He, Z.X., and Yu, Z.Z., *Tough Graphene-Polymer Microcellular Foams for Electromagnetic Interference Shielding.* Acs Applied Materials & Interfaces, 2011. **3**(3): p. 918-924.

23. Thomassin, J.M., Pagnoulle, C., Bednarz, L., Huynen, I., Jerome, R., and Detrembleur, C., *Foams of polycaprolactone/MWNT nanocomposites for efficient EMI reduction.* Journal of Materials Chemistry, 2008. **18**(7): p. 792-796.

24. Lee, L.J., Zeng, C.C., Cao, X., Han, X.M., Shen, J., and Xu, G.J., *Polymer nanocomposite foams.* Composites Science and Technology, 2005. **65**(15-16): p. 2344-2363.

25. VanHouten, D.J. and Baird, D.G., *Generation of Low-Density High-Performance Poly(arylene ether sulfone) Foams Using a Benign Processing Technique.* Polymer Engineering and Science, 2009. **49**(1): p. 44-51.

26. Li, Z.K., Jia, Y.B., and Bai, S.B., *Polysulfone foam with high expansion ratio prepared by supercritical carbon dioxide assisted molding foaming method.* Rsc Advances, 2018. **8**(6): p. 2880-2886.

27. Yang, Q., Zhang, G.C., Ma, Z.L., Li, J.T., and Fan, X.L., *Effects of processing parameters and thermal history on microcellular foaming behaviors of PEEK using supercritical CO2.* Journal of Applied Polymer Science, 2015. **132**(39).

28. *Last-A-foam.* p. https://www.generalplastics.com/products.

29. *Specflex.* p. https://www.dow.com/en-us/product-search/specflexpolyurethanesystems.

30. *Rohacell.* p. https://www.rohacell.com/product/rohacell/en/processing/.

31. *Rogers.* p. https://www.rogerscorp.com/ems/bisco/index.aspx.

32. *Polydamp.* p. https://www.polytechinc.com/products/acoustic-foam.

33. *Solimide.* p. https://www.boydcorp.com/protection/solimide-foams.html.

34. *INTEK.* p. http://www.trelleborg.com/en/applied-technologies/products--and--solutions/thermal--and--acoustic--insulation/intek--pfi--polyimide--foam--insulation.

35. *Gurit.* p. http://www.gurit.com/Our-Business/Composite-Materials/Structural-Core-Materials/Gurit-PVC.

36. *Zotek.* p. https://www.zotefoams.com/product/zotek/.

37. *Important Characteristics of JKSteel.* p. Company literature from Join King Fine Chemical Co., Ltd. .

38. Swier, S., Chun, Y.S., Gasa, J., Shaw, M.T., and Weiss, R.A., *Sulfonated poly(ether ketone ketone) ionomers as proton exchange membranes.* Polymer Engineering and Science, 2005. **45**(8): p. 1081-1091.

39. Carbone, A., Gatto, I., Ohira, A., Wu, L.B., and Passalacqua, E., *Influence of post-casting treatments on sulphonated polyetheretherketone composite membranes.* Journal of Power Sources, 2010. **195**(18): p. 6037-6042.

40. Li, W., Manthiram, A., and Guiver, M.D., *Acid-base blend membranes consisting of sulfonated poly(ether ether ketone) and 5-amino-benzotriazole tethered polysulfone for DMFC.* Journal of Membrane Science, 2010. **362**(1-2): p. 289-297.

41. Gan, D.J., Lu, S.Q., and Wang, Z.J., *Synthesis and characterization of poly(ether ketone ketone) (PEKK)/sodium sulfonated poly(arylene ether ketone) (S-PAEK) block copolymers.* Polymer International, 2001. **50**(7): p. 812-816.

42. Gan, D.J., Lu, S.Q., Song, C.S., and Wang, Z.J., *Morphologies, mechanical properties and wear of poly(ether ketone ketone) (PEKK) and its composites reinforced with mica.* Macromolecular Materials and Engineering, 2001. **286**(5): p. 296-301.

43. Shekar, R.I., Kotresh, T.M., Prasad, A.S.K., Rao, P.M.D., Kumar, M.N.S., and Siddaramaiah, *Hybrid Fiber Fabric Composites from Poly Ether Ether Ketone and Glass Fiber.* Journal of Applied Polymer Science, 2010. **117**(3): p. 1446-1459.

44. Marin-Franch, P., Martin, T., Fernandez-Perez, O., Tunnicliffe, D.L., and Das-Gupta, D.K., *Evaluation of PTCa/PEKK composites for acoustic emission detection.* Ieee Transactions on Dielectrics and Electrical Insulation, 2004. **11**(1): p. 50-55.

45. Guo, M.M., Liu, B.J., Guan, S.W., Liu, C., Qin, H.Y., and Jiang, Z.H., *Novel poly(arylene ether ketone)s containing sulfonic/carboxylic groups: Synthesis and properties.* Journal of Membrane Science, 2010. **362**(1-2): p. 38-46.

46. Converse, G.L., Conrad, T.L., Merrill, C.H., and Roeder, R.K., *Hydroxyapatite whisker-reinforced polyetherketoneketone bone ingrowth scaffolds.* Acta Biomaterialia, 2010. **6**(3): p. 856-863.

47. Tan, S.C., Bai, Z., Sun, H., Mark, J.E., Arnold, F.E., and Lee, C.Y.C., *Processing of microcellular foams from polybenzobisthiazole/polyetherketoneketone molecular composites.* Journal of Materials Science, 2003. **38**(19): p. 4013-4019.

48. Wang, D., Jiang, W., Gao, H., and Jiang, Z.H., *Preparation, characterization, and mechanical properties of microcellular poly(aryl ether ketone) foams.* Journal of Polymer Science Part B-Polymer Physics, 2007. **45**(2): p. 173-183.

49. Kumar, V. and Suh, N.P., *A PROCESS FOR MAKING MICROCELLULAR THERMOPLASTIC PARTS.* Polymer Engineering and Science, 1990. **30**(20): p. 1323-1329.

50. Habibi, S., Nematollahzadeh, A., and Mousavi, S.A., *Nano-scale modification of polysulfone membrane matrix and the surface for the separation of chromium ions from water.* Chemical Engineering Journal, 2015. **267**: p. 306-316.

51. Mahmoudi, E., Ng, L.Y., Ba-Abbad, M.M., and Mohammad, A.W., *Novel nanohybrid polysulfone membrane embedded with silver nanoparticles on graphene oxide nanoplates.* Chemical Engineering Journal, 2015. **277**: p. 1-10.

52. Zhang, L.Y., Zhang, F., Liu, M., and Hu, X., *Novel sustainable geopolymer based syntactic foams: An eco-friendly alternative to polymer based syntactic foams.* Chemical Engineering Journal, 2017. **313**: p. 74-82.

53. Sun, H.L. and Mark, E.J., *Preparation, characterization, and mechanical properties of some microcellular polysulfone foams.* Journal of Applied Polymer Science, 2002. **86**(7): p. 1692-1701.

54. Guo, H.M., Nicolae, A., and Kumar, V., *Solid-state microcellular and nanocellular polysulfone foams.* Journal of Polymer Science Part B-Polymer Physics, 2015. **53**(14): p. 975-985.

55. Guo, H.M., Nicolae, A., and Kumar, V., *Fabrication of High Temperature Polyphenylsulfone Nanofoams Using High Pressure Liquid Carbon Dioxide.* Cellular Polymers, 2016. **35**(3): p. 119-142.

56. Williams, M.K., Melendez, O., Palou, J., Holland, D., Smith, T.M., Weiser, E.S., and Nelson, G.L., *Characterization of polyimide foams after exposure to extreme weathering conditions.* Journal of Adhesion Science and Technology, 2004. **18**(5): p. 561-573.

57. Williams, M.K., Holland, D.B., Melendez, O., Weiser, E.S., Brenner, J.R., and Nelson, G.L., *Aromatic polyimide foams: factors that lead to high fire performance.* Polymer Degradation and Stability, 2005. **88**(1): p. 20-27.

58. Kuwabara, A., Ozasa, M., Shimokawa, T., Watanabe, N., and Nomoto, K., *Basic mechanical properties of balloon-type TEEK-L polyimide-foam and TEEK-L filled aramid-honeycomb core materials for sandwich structures.* Advanced Composite Materials, 2005. **14**(4): p. 343-363.

59. Hshieh, F.Y., Hirsch, D.B., and Beeson, H.D., *Ignition and combustion of low-density polyimide foam.* Fire and Materials, 2003. **27**(3): p. 119-130.

60. Pan, L.Y., Zhan, M.S., and Wang, K., *Preparation and Characterization of High-Temperature Resistance Polyimide Foams.* Polymer Engineering and Science, 2010. **50**(6): p. 1261-1267.

61. Yudin, V.E., Otaigbe, J.U., and Artemieva, V.N., *Processing and properties of new high-temperature, lightweight composites based on foam polyimide binder.* Polymer Composites, 1999. **20**(3): p. 337-345.

62. Pan, L.Y., Zhan, M.S., and Wang, K., *High-Temperature-Resistant Polyimide/Montmorillonite Nanocomposite Foams by Solid Blending.* Polymer Engineering and Science, 2011. **51**(7): p. 1397-1403.

63. Sun, H.L., Sur, G.S., and Mark, J.E., *Microcellular foams from polyethersulfone and polyphenylsulfone - Preparation and mechanical properties.* European Polymer Journal, 2002. **38**(12): p. 2373-2381.

64. Krause, B., Sijbesma, H.J.P., Munuklu, P., van der Vegt, N.F.A., and Wessling, M., *Bicontinuous nanoporous polymers by carbon dioxide foaming.* Macromolecules, 2001. **34**(25): p. 8792-8801.

65. Nemoto, T., Takagi, J., and Ohshima, M., *Nanocellular Foams-Cell Structure Difference Between Immiscible and Miscible PEEK/PEI Polymer Blends.* Polymer Engineering and Science, 2010. **50**(12): p. 2408-2416.

66. Zhou, C., Wang, P., and Li, W., *Fabrication of functionally graded porous polymer via supercritical CO2 foaming.* Composites Part B-Engineering, 2011. **42**(2): p. 318-325.

67. Kim, Y.H. and Li, W., *Multifunctional polyetherimide nanocomposite foam.* Journal of Cellular Plastics, 2013. **49**(2): p. 131-145.

68. Sorrentino, L., Aurilia, M., and Iannace, S., *Polymeric Foams from High-Performance Thermoplastics.* Advances in Polymer Technology, 2011. **30**(3): p. 234-243.

69. Miller, D., Chatchaisucha, P., and Kumar, V., *Microcellular and nanocellular solid-state polyetherimide (PEI) foams using sub-critical carbon dioxide I. Processing and structure.* Polymer, 2009. **50**(23): p. 5576-5584.

70. Li, B., Liu, T., Tang, Z.C.W., and Zhong, W.H., *Fabrication and characterization of flexible high performance thermoplastic foams derived from rigid polyetherketoneketone via a VOC-free foaming method.* Journal of Materials Science, 2013. **48**(9): p. 3517-3527.

71. Mohebbi, A., Mighri, F., Ajji, A., and Rodrigue, D., *Current Issues and Challenges in Polypropylene Foaming: A Review.* Cellular Polymers, 2015. **34**(6): p. 299-337.

72. Strauss, W.C., *SATURATION AND FOAMING OF THERMOPLASTIC NANOCOMPOSITESUSING SUPERCRITICAL CO_2.* Master Thesis, UNIVERSITY OF NORTH TEXAS.

73. Yang, H.H. and Han, C.D., *THE EFFECT OF NUCLEATING-AGENTS ON THE FOAM EXTRUSION CHARACTERISTICS.* Journal of Applied Polymer Science, 1984. **29**(12): p. 4465-4470.

74. Wypych, G. and Wypych, A., *Databook of Nucleating Agents.* 2016: p. Chapter 3.6.5.

75. Lisker, I.S., Solovyev, S.V., Axcell, B.P., Varlow, B.R., and Donnelly, K., *A transient technique for measuring the thermal conductivity of non-metals.* Experimental Thermal and Fluid Science, 2001. **25**(6): p. 377-382.

76. Shi, R.B., Y. Z. Yang, W. X. Wang, D. Wang, J. Y. Jian, X. G., *Optimization and characterization of poly(phthalazinone ether ketone) (PPEK) heat-resistant porous fiberous mat by electrospinning.* Applied Surface Science, 2016. **379**: p. 282-290.

77. Wang, S.J.M., Y. Z.; Hlil, A. R.; Hay, A. S., *Synthesis and characterization of phthalazinone containing poly(arylene ether)s, poly(arylene thioether)s, and poly(arylene sulfone)s via a novel N-C coupling reaction.* Macromolecules, 2004. **37**.

78. N.C. Hilyard, A.C., *Low density cellular plastics*. 1994: Springer Science.

79. Lorna J. Gibson, M.F.A., *Cellular Solids Structure and Properties*. 1999: Cambridge University Press.

80. *Plastics - Thermal Conductivity Coefficients*. Available from: https://www.engineeringtoolbox.com/thermal-conductivity-plastics-d_1786.html.

81. Yablon, D.G., *Scanning Probe Microscopy in Industrial Applications.* WILEY: p. Chapter 2.

82. Sneddon, I., *The relation between load and penetration in the axisymmetric boussinesq problem for a punch of arbitrary profile.* Int. J. Eng. Sci, 1965. **3**: p. 47-57.

83. Oliver, W.C. and Pharr, G.M., *An improved technique for determining hardness and elastic modulus using load and displacement sensing indentation experiments.* J. Mater. Res., 1992. **7**(6): p. 1564-1583.

84. Kurtz, S.M., *UHMWPE BIOMATERIALS HANDBOOK, 3rd Edition*. 2016, William Andrew.

85. Chatterjee, S., McDonald, C., Niu, J., Velankar, S.S., Wang, P., and Huang, R., *Wrinkling and folding of thin films by viscous stress.* Soft Matter, 2015. **11**(9): p. 1814-27.

86. Vandeparre, H., Leopoldes, J., Poulard, C., Desprez, S., Derue, G., Gay, C., and Damman, P., *Slippery or sticky boundary conditions: Control of wrinkling in metal-capped thin polymer films by selective adhesion to substrates.* Physical Review Letters, 2007. **99**(18).

87. Yoo, P.J., Suh, K.Y., Kang, H., and Lee, H.H., *Polymer elasticity-driven wrinkling and coarsening in high temperature buckling of metal-capped polymer thin films.* Physical Review Letters, 2004. **93**(3).

88. Liang, J., Huang, R., Yin, H., Sturm, J.C., Hobart, K.D., and Suo, Z., *Relaxation of compressed elastic islands on a viscous layer.* Acta Materialia, 2002. **50**(11): p. 2933-2944.

89. Vandeparre, H. and Damman, P., *Wrinkling of stimuloresponsive surfaces: Mechanical instability coupled to diffusion.* Physical Review Letters, 2008. **101**(12).

90. Nolte, A.J., Chung, J.Y., Davis, C.S., and Stafford, C.M., *Wrinkling-to-delamination transition in thin polymer films on compliant substrates.* Soft Matter, 2017. **13**(43): p. 7930-7937.

91. Khang, D.-Y., Rogers, J.A., and Lee, H.H., *Mechanical Buckling: Mechanics, Metrology, and Stretchable Electronics.* Advanced Functional Materials, 2009. **19**(10): p. 1526-1536.

92. Chung, J.Y., Nolte, A.J., and Stafford, C.M., *Surface Wrinkling: A Versatile Platform for Measuring Thin-Film Properties.* Advanced Materials, 2011. **23**(3): p. 349-368.

93. Chan, E.P., Smith, E.J., Hayward, R.C., and Crosby, A.J., *Surface wrinkles for smart adhesion.* Advanced Materials, 2008. **20**(4): p. 711-+.

94. Chung, J.Y., Youngblood, J.P., and Stafford, C.M., *Anisotropic wetting on tunable micro-wrinkled surfaces.* Soft Matter, 2007. **3**(9): p. 1163-1169.

95. Krueger, D.L., Bartusiak, J.T., Hanschen, T.P., and Capik, K.M., *Elastomeric laminates with microtextured skin layers*. 1997.

96. Hu, Y., Hiltner, A., and Baer, E., *Buckling in elastomer/plastic/elastomer 3-layer films.* Polymer Composites, 2004. **25**(6): p. 653-661.

97. Li, T. and Suo, Z., *Deformability of thin metal films on elastomer substrates.* International Journal of Solids and Structures, 2006. **43**(7-8): p. 2351-2363.

98. Takei, A., Jin, L., Fujita, H., Takei, A., Fujita, H., and Jin, L., *High-Aspect-Ratio Ridge Structures Induced by Plastic Deformation as a Novel Microfabrication Technique.* ACS Applied Materials & Interfaces, 2016. **8**(36): p. 24230-24237.

99. Gurmessa, B.J. and Croll, A.B., *Onset of Plasticity in Thin Polystyrene Films.* Physical Review Letters, 2013. **110**(7): p. 074301.

100. Semler, M.R., Harris, J.M., Croll, A.B., and Hobbie, E.K., *Localization and length-scale doubling in disordered films on soft substrates.* Physical Review E, 2013. **88**(3): p. 032409.

101. Jin, L., Takei, A., and Hutchinson, J.W., *Mechanics of wrinkle/ridge transitions in thin film/substrate systems.* Journal of the Mechanics and Physics of Solids, 2015. **81**: p. 22-40.

102. Zang, J., Zhao, X., Cao, Y., and Hutchinson, J.W., *Localized ridge wrinkling of stiff films on compliant substrates.* Journal of the Mechanics and Physics of Solids, 2012. **60**(7): p. 1265-1279.

103. Takei, A., Jin, L.H., and Fujita, H., *High-Aspect-Ratio Ridge Structures Induced by Plastic Deformation as a Novel Microfabrication Technique.* Acs Applied Materials & Interfaces, 2016. **8**(36): p. 24230-24237.

104. Yang, J.Y., Damle, S., Maiti, S., and Velankar, S.S., *Stretching-induced wrinkling in plastic-rubber composites.* Soft Matter, 2017. **13**(4): p. 776-787.

105. Zhai, W.T., Feng, W.W., Ling, J.Q., and Zheng, W.G., *Fabrication of Lightweight Microcellular Polyimide Foams with Three-Dimensional Shape by CO2 Foaming and Compression Molding.* Industrial & Engineering Chemistry Research, 2012. **51**(39): p. 12827-12834.

106. Yeh, S.K., Liu, W.H., and Huang, Y.M., *Carbon Dioxide-Blown Expanded Polyamide Bead Foams with Bimodal Cell Structure.* Industrial & Engineering Chemistry Research, 2019. **58**(8): p. 2958-2969.